DISCLAIMER

This report was prepared as an account of work sponsored by an agency of the United States Government. Neither the United States Government nor any agency thereof, nor any of their employees, makes any warranty, express or implied, or assumes any legal liability or responsibility for the accuracy, completeness, or usefulness of any information, apparatus, product, or process disclosed, or represents that its use would not infringe privately owned rights. Reference herein to any specific commercial product, process, or service by trade name, trademark, manufacturer, or otherwise does not necessarily constitute or imply its endorsement, recommendation, or favoring by the United States Government or any agency thereof. The views and opinions of authors expressed herein do not necessarily state or reflect those of the United States Government or any agency thereof. Reference herein to any social initiative (including but not limited to Diversity, Equity, and Inclusion (DEI); Community Benefits Plans (CBP); Justice 40; etc.) is made by the Author independent of any current requirement by the United States Government and does not constitute or imply endorsement, recommendation, or support by the United States Government or any agency thereof.

Exceptional service in the national interest

date: 12/4/2024

to: Neal Hubbard, 2932

from: Ryan Smith and Edmundo Corona, 1558

subject: ***Calibration of AL7075 with Plate-Puncture Predictions***

Introduction

The following details calibration of a material model for Al7075-T6511. This aluminum alloy is commonly used across a host of engineering applications. Owing to its widespread prevalence, there is great benefit in improving simulation predictions for this alloy. In the present effort, a calibration is performed of its elastic-plastic response accounting for both rate and temperature dependence. The calibration is informed by a series of tests that include specimens of different geometries tested at different rates and temperatures. All specimens are derived from the same bar-stock, 3.5 inches in diameter. The fitted model itself uses an anisotropic, Hill yield surface coupled with a Johnson-Cook hardening model. Failure predictions are had by means of a modified Wilkins failure criterion.

Following calibration of the material model, a validation exercise is performed against plate-puncture experiments. These experiments include multiple probe shapes, probe diameters, and plate thicknesses. The puncture experiments are replicated in simulation with mesh studies performed to assess uncertainty. Key quantities of interest, notably the absorbed energy up to failure, are compared between simulation and experiment providing a means to assess the suitability of the calibration in puncture simulations.

Calibration:

Material Characterization Experiments

In gathering experimental data for the calibration, multiple tests are involved. Each test helps characterize a different aspect of the material response. General features of interest include the elastic-plastic response, failure initiation, and dependence of these two on both rate and

Sandia National Laboratories
P.O. Box 5800, MS XXXX
Albuquerque, NM 87185

temperature. A series of tests were devised to query these effects. As essential background for the calibration, a brief summary of the experimental tests follows below.

Uniaxial Tension

The plastic response is calibrated through uniaxial tension tests. Tension tests were performed at room temperature as well as at 50 ºC and 100 ºC. Drawings for the uniaxial tension specimen are provided in Appendix B. To summarize key geometrical features, the tension specimen is a standard dog-bone with test section diameter of 0.25” and effective length of 0.750”. Displacements are measured with an extensometer of gage length 0.5”.

As a brief digression, several comments are made on the stock material. Most importantly, all test specimens are cut from a single bar stock. This cylindrical bar-stock is cut into multiple smaller sub-lengths. From each sub-length, multiple tensile specimens are cut. Tensile specimens derive from both different sub-lengths as well as from different locations within a given cross-section. Furthermore, samples are included both with their tensile axis aligned to the axis of the bar as well as with their tensile axis oriented at 90 degrees to the axis of the bar. This information is summarized in the drawings found in Appendix B.

Most of the tension tests are performed at a quasi-static strain rate of 1.6E-04 1/s. Several additional tests are run at an intermediate rate of 3.3E-02 1/s. Taken together, these tests provide information on the plastic behavior of the material with some limited insight into temperature and rate dependence. Further, the inclusion of specimens from varying regions and orientations throughout the stock material will aid in characterizing yield anisotropy. Plots of engineering stress vs engineering strain are presented in Figure 1.

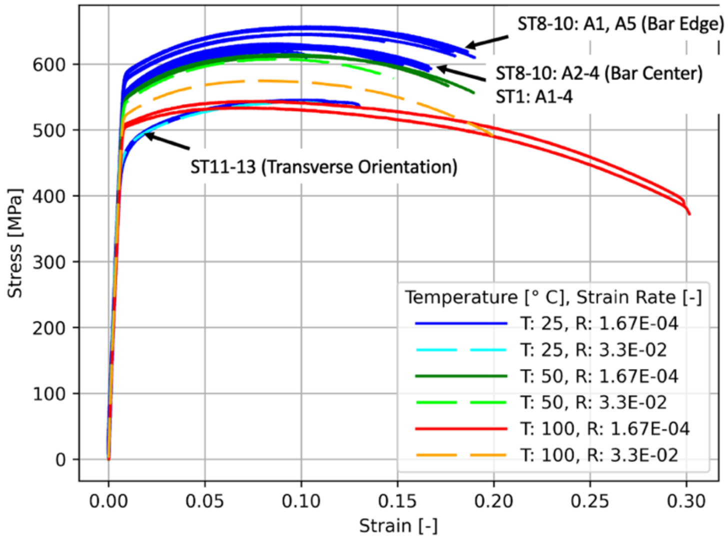

Figure 1. Engineering stress vs engineering strain is plotted for all experimental-tension tests including room temperature (25 ºC), 50 ºC, and 100 ºC as well as for rates of 1.67E-04 1/s and 3.3E-02 1/s

A large spread is noted in the room-temperature tests. Specimens cut from the edge of the bar stock (see Appendix B) show a higher flow stress compared to those cut from the center. In contrast, specimens cut with their tension axis transverse to the axis of the bar stock show a much lower flow stress indicating yield anisotropy in the material. Despite apparent variance as regards tensile orientation and specimen radial location, focus is placed on those specimens cut from the center of the bar and with their tension axis oriented parallel to the axis of the bar. The present calibration will focus on these cases while taking note of the anisotropy.

As for temperature effects, higher temperature decreases the flow-stress and extends the strain to failure. Compared to room-temperature, the tension tests performed at 100ºC show a 50% increase in failure strain. The influence of rate is less perceptible. Going from 1.67E-4 to 3.3E-2 1/s, the flow plastic behavior appears largely unchanged at 25 and 50ºC although the failure strain is slightly reduced. The effect of strain rate is more significant at 100ºC

In terms of the material calibration, these tension tests serve primarily to inform the hardening function of the plasticity model which includes a Hill yield function that hardens isotropically. Failure behavior, in contrast, is better informed by notch and hat tests. Notch tests are discussed next.

Notch Tension

Tension specimens with varying notch radii are used to characterize the failure behavior of the material. The inclusion of several notch radii yields information on the influence of triaxiality where, in general, a smaller notch radius leads to a state of higher triaxiality.

Specimens with notch radii of 0.032, 0.064, 0.128, and 0.320 inches with cross-sectional radius of 0.125 inches, are tested. For each geometry, several tests are performed to demonstrate repeatability. As before, all specimen drawings are found in Appendix B.

Experiments are performed quasi-statically with cross-head displacement rate varying depending on notch radii to approximate the strain-rate in the slowest uniaxial tension test. Cross-head displacement rates are 0.011, 0.021, 0.043, and 0.085 mil/s for specimens with notch radii of 0.032, 0.064, 0.128 and 0.320 inches respectively. Excepting the 0.320” notch, a 0.5” extensometer measures displacement across the notch. For the 0.320” specimens, a 1.0” extensometer is used. Experimental load displacement is plotted in Figure 2. Some variation is evident in the experimental results, becoming more significant for smaller notch sizes.

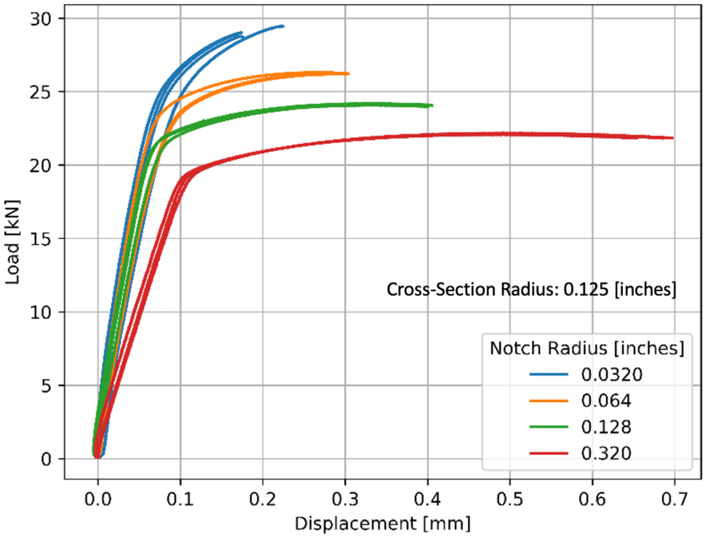

Figure 2. Load vs displacement is plotted for the notch specimens, which were run at room temperature and at a quasi-static rate.

Notch specimens provide a wealth of information for the failure calibration. Further characterization is provided via hat-compression tests discussed next.

Hat Compression

Hat compression tests provide additional information to characterize the failure response. As the reader may be unfamiliar with this experiment, Figure 3 demonstrates the essential setup. In this experiment a “hat” specimen is compressed between two platens. A region of high shear develops in the noted ligament where failure is expected to initiate from either the top or bottom faces. Compared to the notch tests, the hat specimen induces a compressive hydrostatic stress alongside the more-obvious shear. It is the combination of compressive stress and high shear that differentiates the hat from the notch specimens providing a unique data point from which to calibrate. Drawings for the hat specimen are found in Appendix B. Load displacement results for the hat specimens are plotted in Figure 4. The compression rate was 0.1 mil/s oriented along the bar axis. Tests show good repeatability.

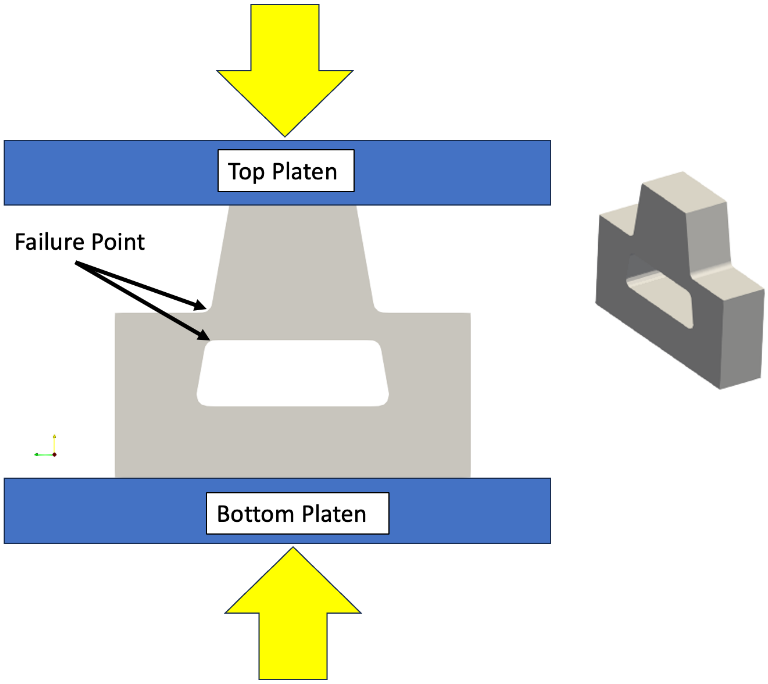

Figure 3. The basic setup of the hat-compression test is shown

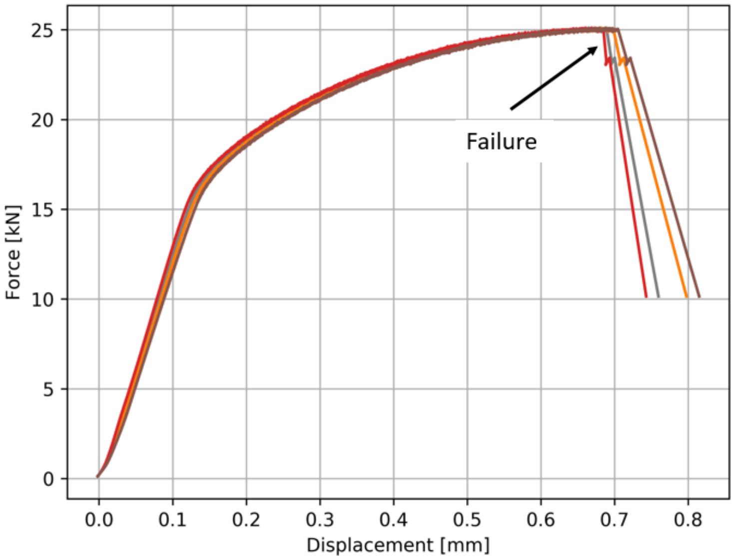

Figure 4. Load vs displacement is plotted for all hat tests. Experiments were conducted at room temperature and quasi-static rate.

Kolsky Bar Tension

Rate dependence is explored via Kolsky bar tests. Specimen dimensions are again included in the appendix. From a calibration perspective, the key takeaway is that three additional strain rates are tested, each at room temperature. The tested strain rates are 500 1/s, 1000 1/s, and 3000 1/s. Stress-strain curves for each are presented in Figure 5. Rate dependence is limited with flow-stress remaining largely similar across all cases. Though the failure point is not as well defined, higher rate appears to fail at smaller strains as suggested by the earlier drop in load. Note all specimens are oriented in the axial direction.

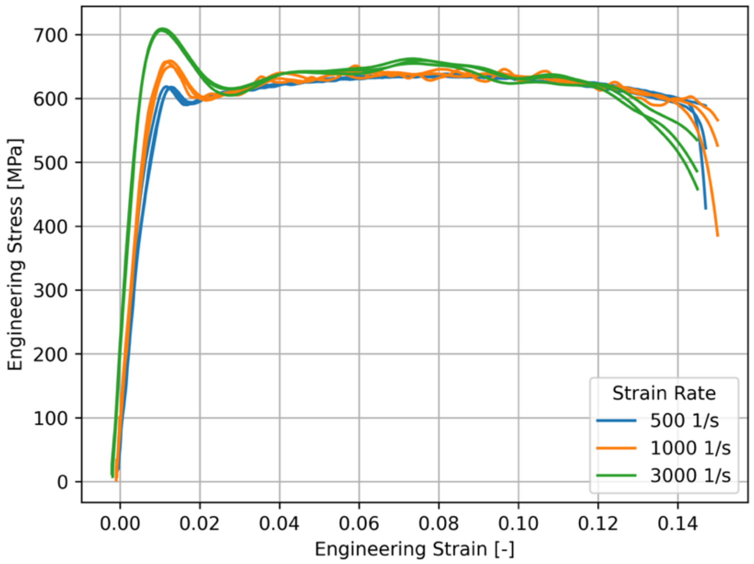

Figure 5. Stress-strain curves from Kolsky bar experiments are plotted for three different strain rates

Constitutive Model

Above summarizes the material response across all the tests. Attention is now turned to modeling. This effort makes use of LAME's recent work in modular constitutive models which allows for the mixing and matching of various plasticity and damage models. Here, a Hill yield surface is selected with a power-law hardening behavior. For rate dependence, a Johnson-Cook relationship is used. Temperature dependence is defined according to a user function. Coupled with this plasticity model is a Wilkins failure model which itself allows for rate and temperature dependence. A brief summary is provided.

The Hill yield surface is anisotropic. For brevity, equations are not reproduced here. Equations defining the Hill yield surface can be found in the LAME manual [1]. Relevant to this calibration effort, seven parameters are needed to define the yield surface. These are a reference yield stress, $\bar{\sigma}$, plus six parameters that give the ratio between this reference yield stress and a yield stress for each component of the stress tensor in the axes of principal anisotropy. Notationally, these parameters are written

$$R_{ij} = \begin{Bmatrix} \dfrac{\sigma_{ij}}{\bar{\sigma}}, & i = j \\ \sqrt{3}\dfrac{\sigma_{ij}}{\bar{\sigma}}, & i \neq j \end{Bmatrix} \qquad 1.$$

When all R_{ij} equal 1.0, the Von-Mises yield criterion is recovered.

Coupled with this yield surface is a Johnson-Cook hardening law following the form

$$\bar{\sigma} = \left[A(T) + B(\bar{\epsilon}^p)^{N(T)}\right][1 + C < \ln\left(\frac{\dot{\bar{\epsilon}}^p}{\dot{\epsilon}_0}\right) >] \qquad 2.$$

where A is the initial yield stress, B is the hardening modulus, N the hardening constant, C the rate constant, $\dot{\bar{\epsilon}}^p$ a plastic strain rate, $\dot{\epsilon}_0$ a reference strain rate, and T the temperature. Note A, B, and N are all permitted to vary with temperature. This hardening law, coupled with the Hill yield surface defines the plastic behavior.

Now considering the failure model, an extended form of the Wilkins failure criteria is adopted [2][3] following the form

$$d = \frac{1}{d_{crit}} \int w_1(\sigma_m) w_2(\theta) w_3(\dot{\bar{\epsilon}}^p) w_4(T) d\hat{\epsilon}^p \qquad 3.$$

where d is a dimensionless damage value, d_{crit} a critical damage parameter, and the parameters w_i dimensionless functions of the mean-stress, lode angle, strain rate, and temperature. Integration is performed over the plastic strain. Failure is defined when the damage, d, equals one.

The parameter w_1 is calculated as

$$w_1 = \left(\frac{1}{1 - \frac{\sigma_m}{B}}\right)^{\alpha} \qquad 4.$$

where σ_m is the mean stress and B and α are parameters to be calibrated. The second parameter, w_2, implicitly accounts for lode angle dependence and takes the form

$$w_2 = (2 - A)^{\beta} \qquad 5.$$

where β is a calibration parameter and A equals

$$A = \max\left(\frac{s_2}{s_3}, \frac{s_2}{s_1}\right) \tag{6.}$$

where s_i are the principal values of the deviatoric stress tensor.

Similar to the plasticity model, rate dependence is incorporated via a Johnson cook-type form with w_3 calculated as

$$w_3 = \frac{1}{1 + D_4 \ln\left(\frac{\dot{\bar{\epsilon}}^p}{\dot{\epsilon}_0}\right)} \tag{6.}$$

where D_4 is a calibration parameter, $\dot{\epsilon}_0$ is a reference rate (the same used for the plasticity model), and $\dot{\bar{\epsilon}}^p$ is the plastic strain rate.

Finally, explicit temperature dependence is included through w_4. In the present case, this parameter will be defined through user-functions of temperature. With this, the constitutive model is laid out. In total, four temperature dependent parameters must be defined for the plasticity model and four for the failure model plus a function of temperature. Ideal values for each parameter are determined through the calibration process described below.

Material Calibration

From a high-level, the calibration approach is broken into several steps. First, the plastic response is calibrated assuming no rate or temperature effects. From here, damage can be calibrated, again neglecting rate and temperature. The resulting fit is an intermediate step that serves as a base for the larger calibration. Having this in hand, temperature effects are built into the plasticity model followed by rate. Finally, the calibration concludes with temperature and rate effects worked into the damage model. Each of the above steps are discussed in individual detail below. Comparison between experiment and the calibrated material is presented across several plots in the "Calibration Summary" section. A full Sierra/SM input deck for the material model is included in Appendix C.

Plasticity Calibration

The first step in the calibration procedure aims to fit the plastic response at room temperature and neglecting rate dependence. For this purpose, the essential experiments are the quasi-static, room-temperature tensile tests on specimens oriented axially and taken from the center of the bar stock. A finite element model is developed mimicking the tensile experiments. An example model is shown in Figure 6.

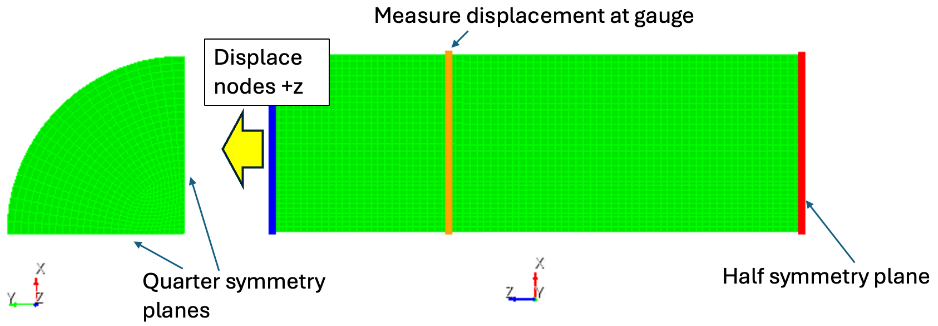

Figure 6. A quarter symmetry model is used for simulating the tensile response

The model uses quarter symmetry boundary conditions along the tensile axis as well as an additional symmetry plane perpendicular the tensile axis that further splits the geometry in half. In simulation, displacements are measured along a series of nodes inserted at a position to match the extensometer in the tests. The model itself extends beyond the gage length, including geometry up to the “points of tangency” where the tensile coupon transitions from a constant cross-sectional radius into the characteristic “dog-bone” shape.

Assuming zero rate and temperature dependence, the plastic hardening model (equation 2) reduces to the following form,

$$\sigma_y = \sigma_y^0(T) + A(T)(\bar{\epsilon}^P)^{n(T)}|_{T=T_{room}} \qquad 7.$$

where σ_y^0 is the initial yield stress taken at the proportional limit, A is the hardening constant, and n is the hardening exponent, all evaluated at room temperature.

Recall the effective stress is based on a Hill yield surface which includes the constants R_{ij}. For the present purposes, all R_{ij} components are set to one excepting R_{23} and R_{31} on which are imposed the restriction R_{23} equals R_{31}. Therefore, only a single additional parameter enters into the calibration on account of the Hill yield surface. In total, the parameters to be calibrated at this stage are $\bar{\sigma}$, A, n, and R_{31}.

The plasticity calibration takes an iterative approach. Starting with an initial guess at the material constants, the tensile simulation is run and the predicted load-displacement compared to that of experiment. Depending on fit, the material constants are adjusted, and the simulation rerun. This continues until an acceptable fit is achieved.

Though tensile specimens are the primary driver for the plasticity calibration, comparison is also made to the hat and notch tests to ensure a reasonable fit across all cases. Initial efforts, which used an isotropic yield surface, found poor alignment between simulation and experiment for the notch and hat compression despite a good fit to the tension tests. The anisotropic yield surface was adopted to help alleviate this issue.

Following this approach, the final fitted parameters for the plasticity model are presented in Table 1. Comparison between simulation and experiment, for both notch and tension, is shown in Figure 7. Note, details of the notch simulation setup are deferred to the next section which focuses on the damage calibration. Simulation predictions show better alignment for the tensile specimen and large radius notch with comparison deteriorating somewhat as notch radius decreases.

Table 1. Calibrated plasticity parameters

σ_y^0 [MPa]	A [MPa]	n [-]	R_{31} [-]
509	394	0.33	0.83

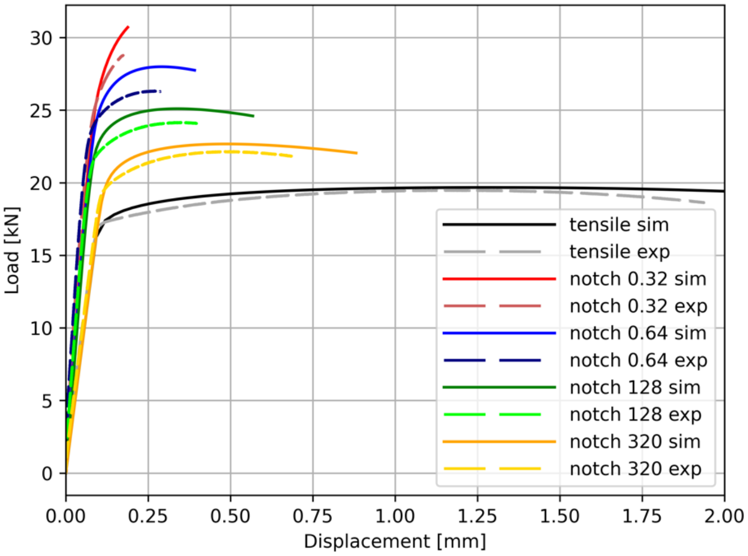

Figure 7. Comparison between experiment and simulation is plotted for tension and for each of the notch tests. Failure is not present in the model at this stage

Above concludes the plasticity calibration for the model at room temperature and with no rate dependence. Next follows the damage calibration under similar conditions.

Damage Calibration

As with the above plasticity calibration, this initial damage calibration will temporarily neglect any rate or temperature effects. For this effort, the essential experiments include both the notch specimens as well as the hat specimen. Simulations are constructed mimicking the experiments for each specimen type. The model setup for each is discussed.

Model Setup

First to discuss the notch specimens, finite element models are developed for each of the four notch radii. Similar to the tension model, 1/8th symmetry is used as seen in Figure 8. The geometry includes up to the extensometer gage length but does not extend further. The top-most surface, at the gauge length, is displaced upwards at quasi-static rate in accord with strain-rates detailed in the experiments section. Based on prior mesh studies [2], 20 elements are maintained through the smallest radius as shown in Figure 9.

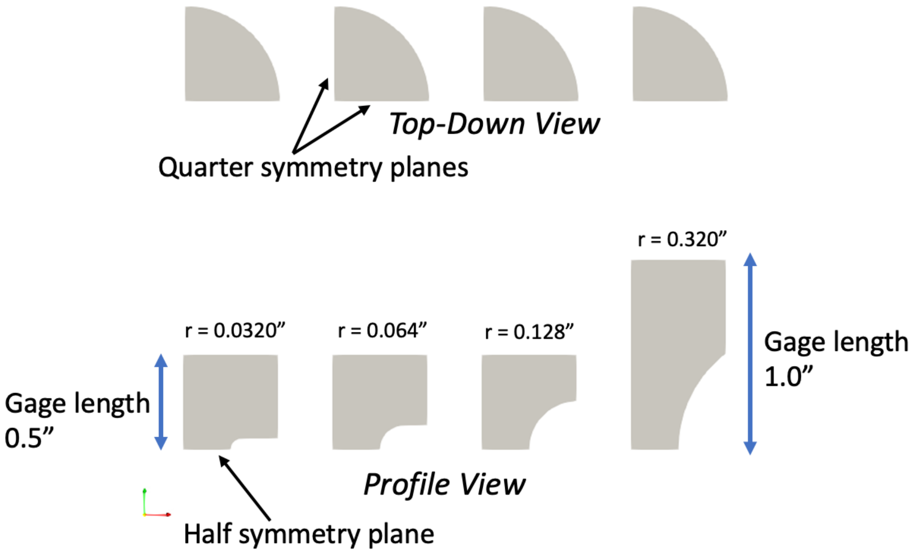

Figure 8. Four notch models are developed for four different radii

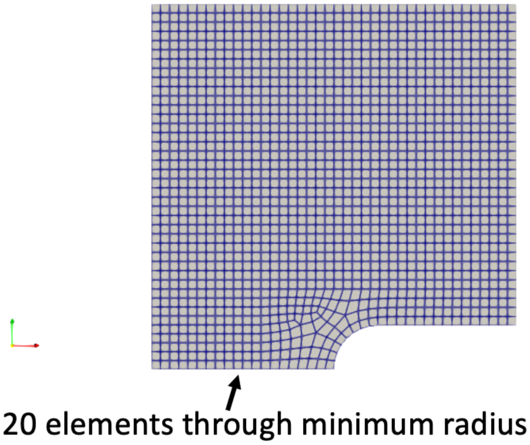

Figure 9. Mesh for the 0.0320 notch is shown. Across all notches, a minimum of 20 elements in maintained through the smallest radius

Moving to the hat specimen, this model uses quarter symmetry as seen in Figure 10. The boundary conditions for the hat specimen are as follows:

- Bottom surface is fixed for all DOF except the vertical direction
- Top surface is fixed in all DOF
- Bottom surface is displaced upwards, putting the specimen in compression

- The remaining boundaries are either free or constrained by symmetry boundary conditions.

Mesh refinement is increased in the region where failure is anticipated. The element edge length in this region is around 0.05 mm.

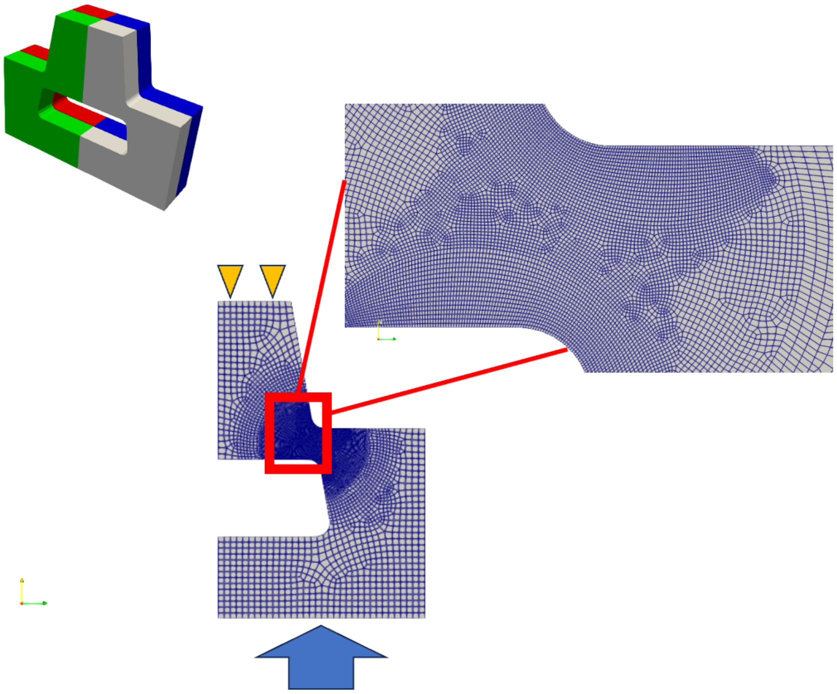

Figure 10. Hat model is shown with mesh

Damage Calibration Procedure

The failure calibration, which uses both hat and notch specimens, is performed with the aid of a Fortran script that implements the procedure in [2]. For this calibration method, each test is simulated first with the principal stresses and equivalent plastic strain output at every step. This script then sweeps through different damage-parameter combinations and, for each, calculates damage values for select elements on the mesh. In doing so, a failure strain is predicted based on the first element to reach a damage value of one. Parameter combos are ranked according to the error between predicted failure-displacement and experimental failure-displacement. From this ranking, a combo is selected which suitably minimizes error across all notch and hat specimens.

Damage parameters selected through this process are in Table 2. Failure predictions for the notch and hat specimens may be seen in Figure 14 and Figure 15 respectively, included in the "Calibration Summary" section.

Table 2. Damage calibration parameters

Parameter	Value
B	4.0e9
α	7.85
β	0.8
d_{crit}	0.5

Temperature and Rate Plasticity Calibration

At this point, the calibration includes damage and plasticity for room-temperature and quasistatic rate. From here, temperature dependence is worked into the plasticity calibration. The relevant experimental tests are the quasi-static tensile tests performed at temperatures of 50C and 100C. For both temperatures, a unique hardening function is calibrated following the same process as for the room-temperature calibration. Fitted parameters are included in Table 3 and load displacement plotted in Figure 11.

Table 3. Calibrated plasticty parameters for temperature of 50ºC and 100ºC

Temperate (ºC)	σ_y^0	A	n
50	404.0	426.0	0.196
100	253.0	476.0	0.131

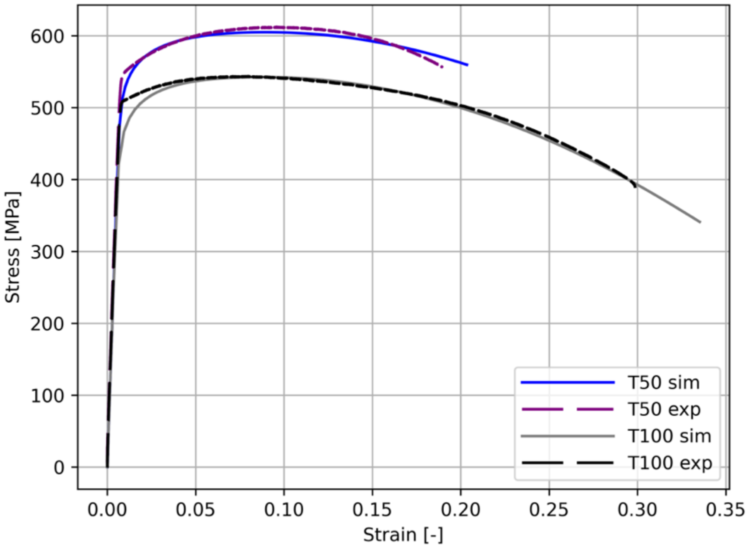

Figure 11. Two additional plasticity calibrations are performed at temperatures of 50 C and 100C

With the addition of fits to 50C and 100C, there are now three plasticity calibrations including the initial room temperature fit. These three are combined into a single calibration by introducing a linear interpolation, over temperature, for each $\sigma_y^0(T)$, $A(T)$, and $n(T)$. Temperature dependence is ensured to be monotonic for each parameter.

With temperature dependence incorporated, rate effects can be addressed. Recall, a Johnson-Cook rate dependence is used which requires calibration of the rate constant, C, as in equation 2. The reference rate is taken to be the quasi-static strain rate for the tensile specimens or 1.6E-04. In addition to the rate constant, the Taylor-Quinney coefficient enters as a second parameter to calibrate. Relevant experiments are the Kolsky bar tests. A matching finite element model is developed with the setup shown in Figure 12. Here it is especially important that the proper displacement-rate be applied to the model. For this purpose, experimentally measured outputs of displacement, which capture the time history, are used to drive the model. Displacements are imposed at the top-most surface which coincides with the experimental gauge length. Remaining boundary conditions are simplistic employing the same symmetry planes as with the tension and notch models. An adiabatic assumption is adopted.

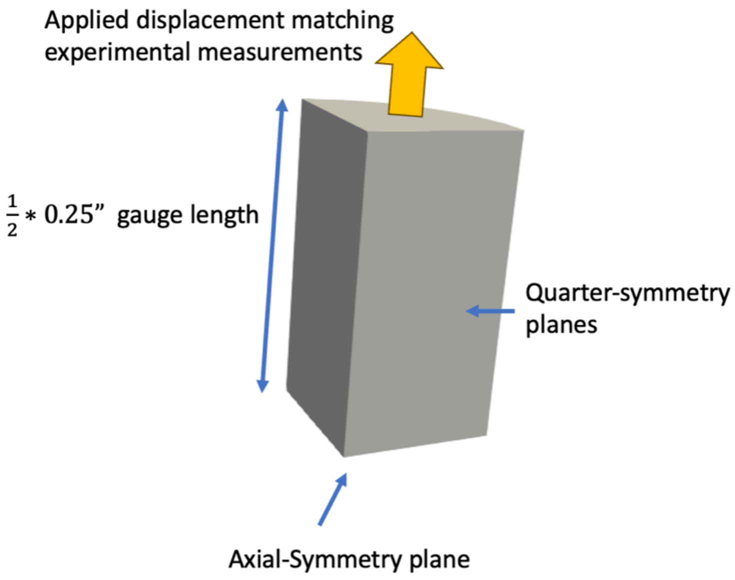

Figure 12. Simulation setup is shown

It should be noted that, before running any simulations, a good estimate for the rate multiplier is attained by simply comparing the experimental curves. The ultimate tensile stress (UTS) provides a useful data point for which to fit the Johnson-Cook function. Starting from this initial guess, simulations are run to verify the fit. Adjustments are made on a trial-and-error basis until an acceptable fit is achieved. Calibrated values are given in Table 4. The specific heat is included for reference though is not part of the calibration.

Table 4. Calibrated rate constant and Taylor-Quinney coefficient

Parameter Name	Parameter Value
C (rate-constant) [-]	0.002
β [-]	0.8
Specific Heat [J/kg-K]	900

Temperature and Rate Dependent Damage

Rate and temperature effects are now included in the plasticity model. The same must be done for the failure model. For temperature dependence, a user defined failure multiplier is defined which takes the place of w_4 in equation 3. Calibration of this parameter is quite simple. Again, relying on the tension tests at 50 ºC and 100 ºC, for each temperature, a failure multiplier is set so that the simulated failure strain matches that in experiment. As the simulations assume constant temperature, the failure multiplier is easily set by considering the ratio of current to desired failure strain and adjusting accordingly. As before, a linear interpolation provides a single temperature dependent failure multiplier. The failure multiplier for each temperature is summarized in Table 5.

Table 5. Failure multiplier is listed for 25ºC, 50ºC, and 100ºC

Temperature (ºC)	w_4
50	0.93
100	0.29

Rate dependence takes a similar approach. Here we again consider the high-rate Kolsky bar tests. Initial simulations are run to attain the predicted failure strain. Depending on discrepancy between predicted and observed failure strain, a rate multiplier, this time following a Johnson-Cook law as in equation 6, is set to shift predictions closer to experiment. The specific parameter set here is D_4. The reference rate is the same as the plasticity model, 1.6E-04. As with setting the temperature failure multiplier, this parameter is well estimated without running any simulations just by assuming an approximate strain rate. From here, further iterations can be made within simulation until the predictions are within reasonable alignment. The calibrated D_4 value is -0.015.

With this, the full calibration is complete. The following section includes a series of plots showing comparison between the calibrated material model and experiment. This is included to both verify the calibration and to summarize its performance against the calibration experiments.

Calibration Summary

The full material card for the calibrated Al7075 model is included in Appendix C. How the model compares to the calibration experiments is summarized across Figure 13-Figure 16. All plots are generated with rate and temperature dependence turned on as verification for these portions of the model. Adiabatic heating is turned off for quasi-static tests and turned on only for the high rate.

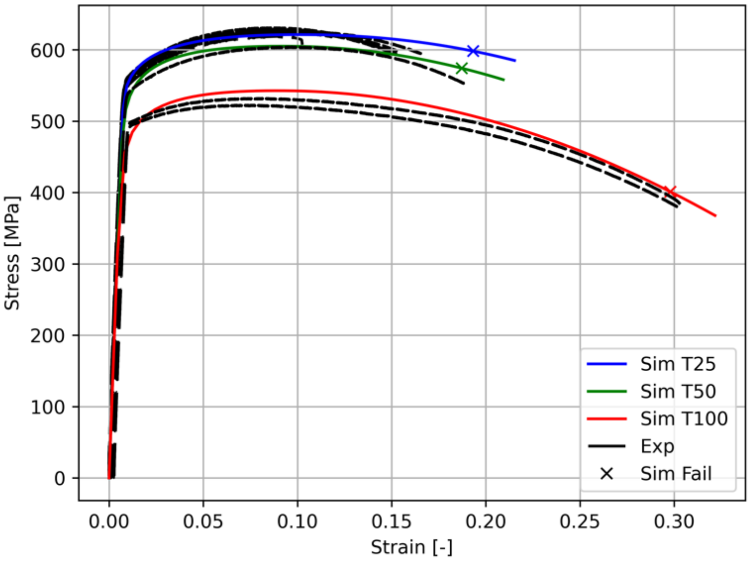

Figure 13. All tension simulations are plotted alongside their experimental counterparts. Predicted failure is marked with an 'x'

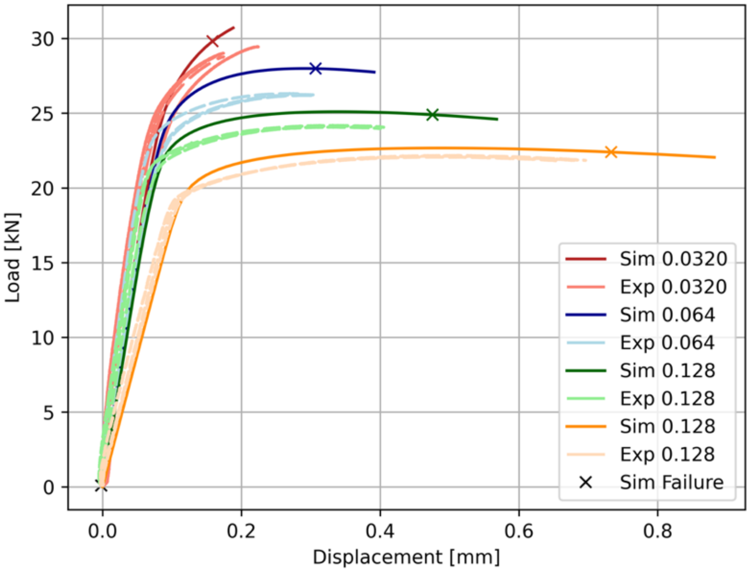

Figure 14. Load-displacement compared between simulation and experiment for each of the three notch radii. Predicted failure is marked with an 'x'

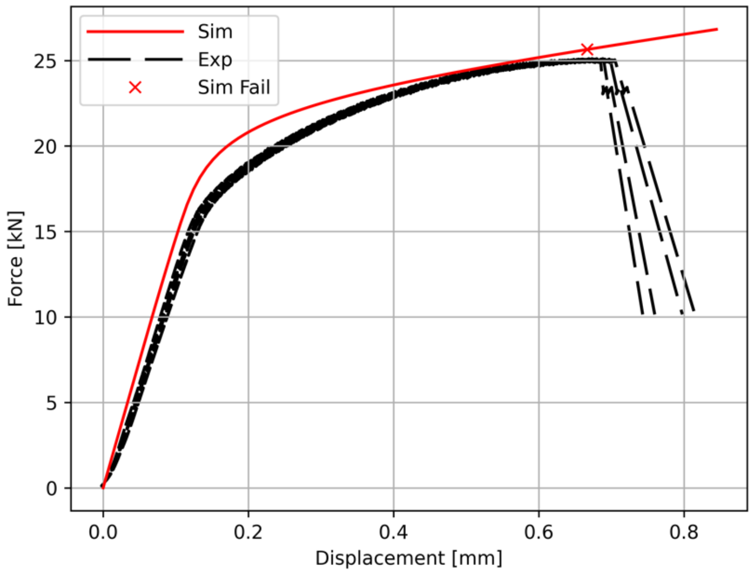

Figure 15. Load-displacement is compared between simulation and experiment for the hat specimen. Predicted failure is marked with an ‘x’

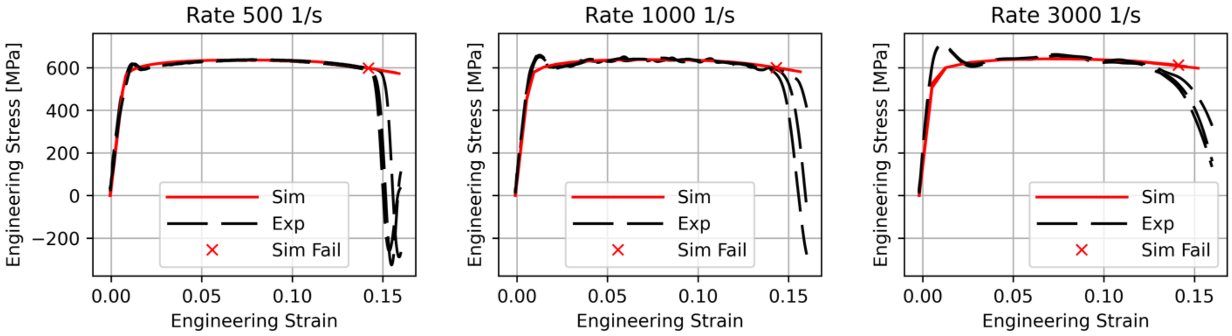
Rate 500 1/s
Rate 1000 1/s
Rate 3000 1/s

Figure 16. Stress vs strain is plotted comparing simulation and experiment for the high-rate tests. Predicted failure is marked with an ‘x’

Late in the process, an oversight was discovered in the Hill yield surface calibration. Specifically, the Hill constants R11, R22, and R12 were meant to be selected so as to better fit the anisotropic behavior evident in Figure 1. Instead, these were mistakenly set to their default values of 1.0 and as such the yield surface is not well suited to capture flow behavior in the transverse direction. The puncture simulations, discussed below, were run prior to this discovery. Rather than rerunning all results, the correction is implemented and addressed in Appendix A. In this appendix section, a limited series of results are rerun to demonstrate sensitivity to this correction. Based on the rerun results, the corrected yield surface shows marginal impact. Thus, the results presented here are considered representative.

Puncture Tests

A series of plate-puncture experiments are conducted, and corresponding simulations run. In these tests a probe attached to a drop table impacts a plate lying below. Given sufficient energy, the probe punctures the plate. The plates used here are cut from the same stock material as the calibration specimens described above. Hence, for simulation purposes, the material calibration applies. A measure of validation is provided comparing between simulation and experiment. Of particular interest is whether the simulations can predict the amount of energy absorbed by the plates. For more details on the experimental setup see [2].

Several punches of varying size and shape are used. The three shapes involved are referred to as “flat”, “blunt”, and “tri-corner” with each pictured in Figure 17. For each shape, diameters of 0.5 and 1.0 inches are tested with an additional 0.25 inch diameter for the flat punch. Plates are made in three different thicknesses: 0.051, 0.114, and 0.250 inches.

An example of the simulation setup is shown in Figure 18. Included in the model is the base, which holds up the plate; the plate itself; the punch; and a cylinder representing the carriage mass, with its density adjusted to match the mass used in the drop table experiment: 138.5 kg. Symmetry is applied where appropriate. Specifically quarter symmetry is used across all flat punch simulations while 1/3rd symmetry is used for all corner punch simulations. For the blunt punch quarter symmetry is used with plate thicknesses of 0.250” and 0.114”. However, no symmetry is modeled for the thinnest plate of 0.051”. Outside of the plate, generic elastic properties for steel are assumed.

At the start of the simulation, the probe is positioned slightly above the plate. An initial velocity is applied to the probe and is taken from experimental readings directly before impact. Further, an “effective gravity” is applied in the simulations to capture the net acceleration acting on the combined probe and mass. Owing to friction in the drop tower frame as well as other loss sources, this applied acceleration does not equal the gravitational constant. As with the initial velocity, the effective gravity is calculated from experimental data as the slope of the velocity vs time plot prior to impact.

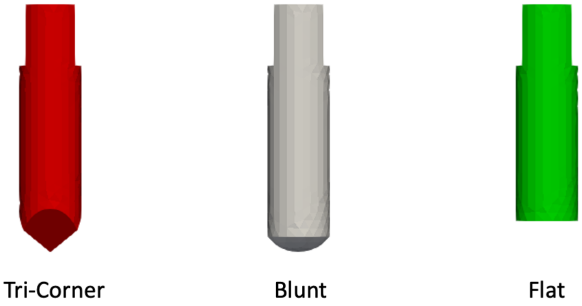

Figure 17. Three different probe shapes are tested (and simulated)

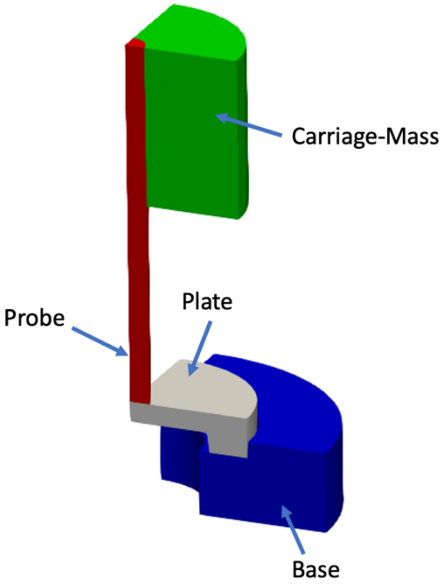

Figure 18. An example model as used in simulation is shown. Note the quarter symmetry.

As the simulation progresses, element death is used to delete elements which have reached the damage criteria. Through this mechanism, “cracks” may propagate allowing the probe to puncture through the plate.

Quantities of interest for these simulations are the acceleration-time history, the velocity-time history, and the energy absorbed by the plate during the impact. The absorbed energy is calculated as the difference in kinetic energy and potential energy just before and after the puncture event. For calculating the kinetic energy, all that is needed is the velocity before and after impact since the carriage and punch masses are known. Velocities are easily read from experimental or simulation output.

The change in potential energy is calculated using the “effective gravity” detailed above. As a simplifying assumption, the effective gravity is assumed to remain constant over the course of the impact. The remaining component needed to calculate the potential energy is the height change. This is calculated as the integral of the velocity over the duration of the puncture event and is computed numerically on both simulation and experimental results. The net change in energy is assumed to come from deformation and fracture of the plate. Hence in calculating these two values, we have an estimate for energy dissipated by the plate.

This calculation depends on how the beginning and end of the puncture event are defined. The puncture is observed as a reasonably well-defined acceleration pulse. A qualitative assessment is made to pick points corresponding to the beginning and end of this pulse-feature. With several exceptions, both the start and end of the pulse are well defined. Several examples are provided in Figure 19.

The above calculation gives an estimate for work done up to the point where the probe tip has completely passed through the plate. This includes all energy expended to propagate cracks and friction between the punch and perforated plates in the experiments. However, crack propagation is inevitably mesh sensitive. A more stable metric might be the work needed to initiate failure prior to any propagation. The initiation point, however, is not well defined. As balance between the two, an alternative metric is the work up to the peak acceleration. The peak-acceleration is a well-defined feature across simulation and experiment and occurs at a time where comparatively less crack propagation has transpired. Several examples are again included in Figure 19 showing how this point is selected.

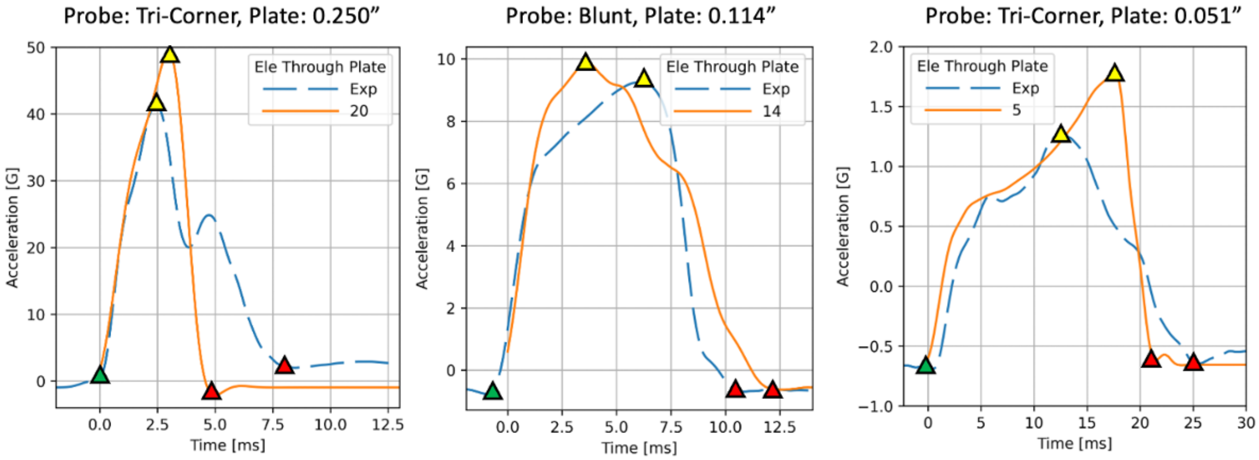

Figure 19. Absorbed energy is calculated across (1) the entire puncture event and (2) up to the peak-acceleration. Several cases are shown for example. Green triangles represent the beginning of the acceleration pulse, yellow triangles the peak acceleration and red triangles the end of the acceleration pulse.

Mesh Study

Mesh studies are conducted for all probes with a diameter of 0.5” across all plate thicknesses. Results are organized according to plate thickness. Acceleration and velocity time histories are plotted for the thick plates (0.250”) in Figure 20. Multiple mesh sizes are compared, with each defined according to elements through the plate thickness. Experimental results are plotted alongside simulation and are included as dashed lines. All simulation results are low-pass filtered at 500 Hz. The same series of plots are generated for plate thicknesses of 0.114” and 0.051” and are included as Figure 22 and Figure 24 respectively. Absorbed energy is summarized across all mesh studies in Table 6.

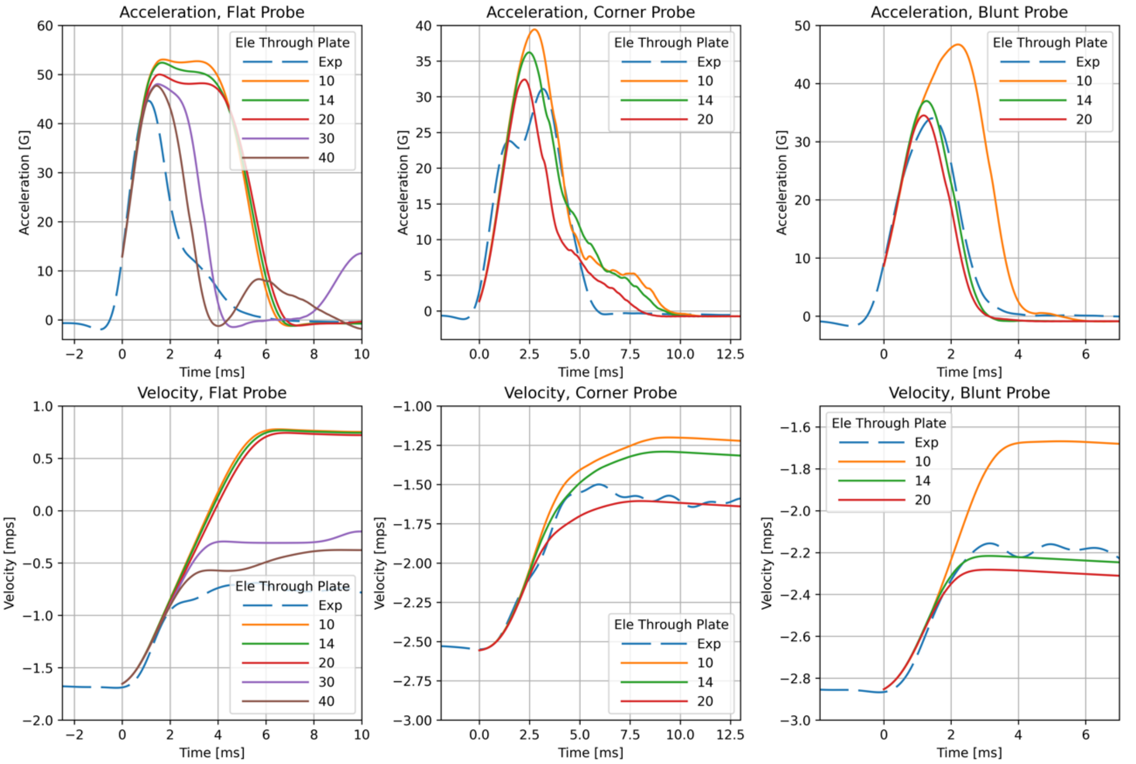

Figure 20. Acceleration and velocity time histories are plotted for plates of thickness 0.250 inch comparing varying number of elements through the plate thickness. Elements were of nominal unit aspect ratio.

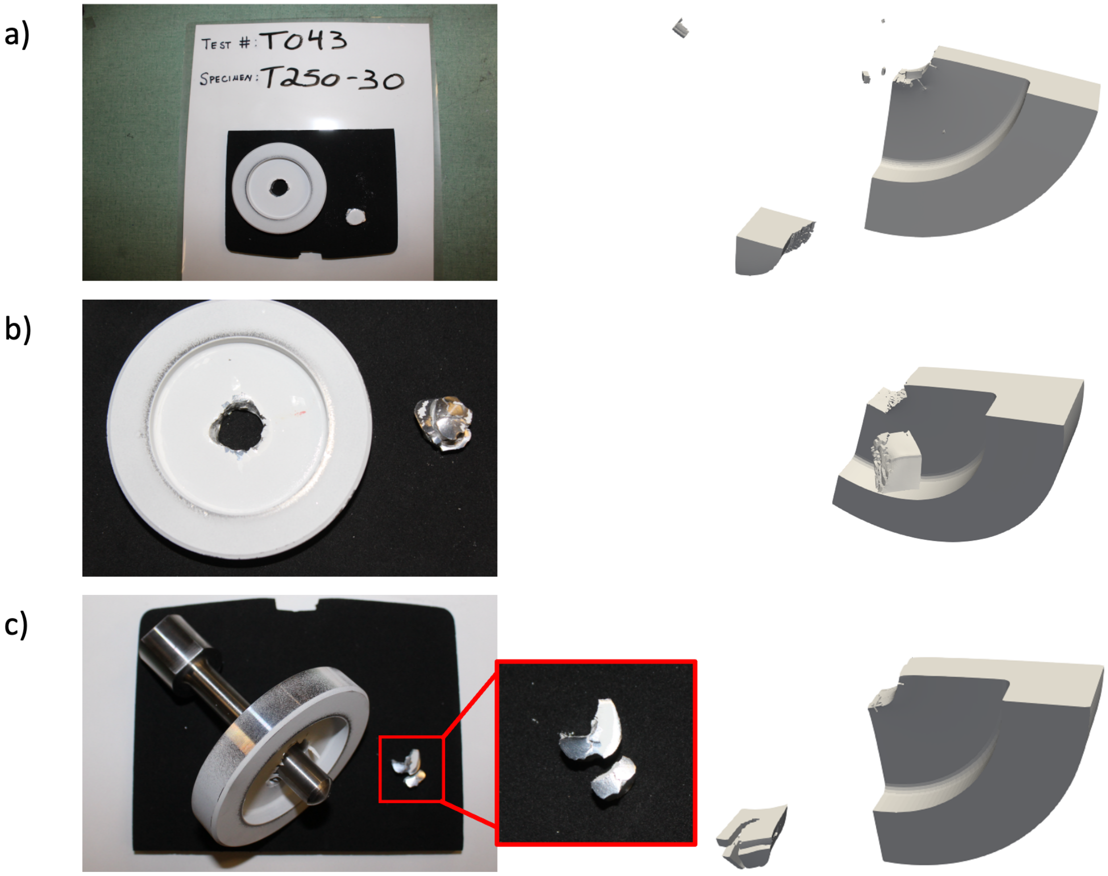

Figure 21. A qualitative comparison is made between 0.250 inch plates, post-puncture, comparing simulation and experiment. Flat probes are compared in (a), tri-corner probes in (b), and blunt probes in (c).

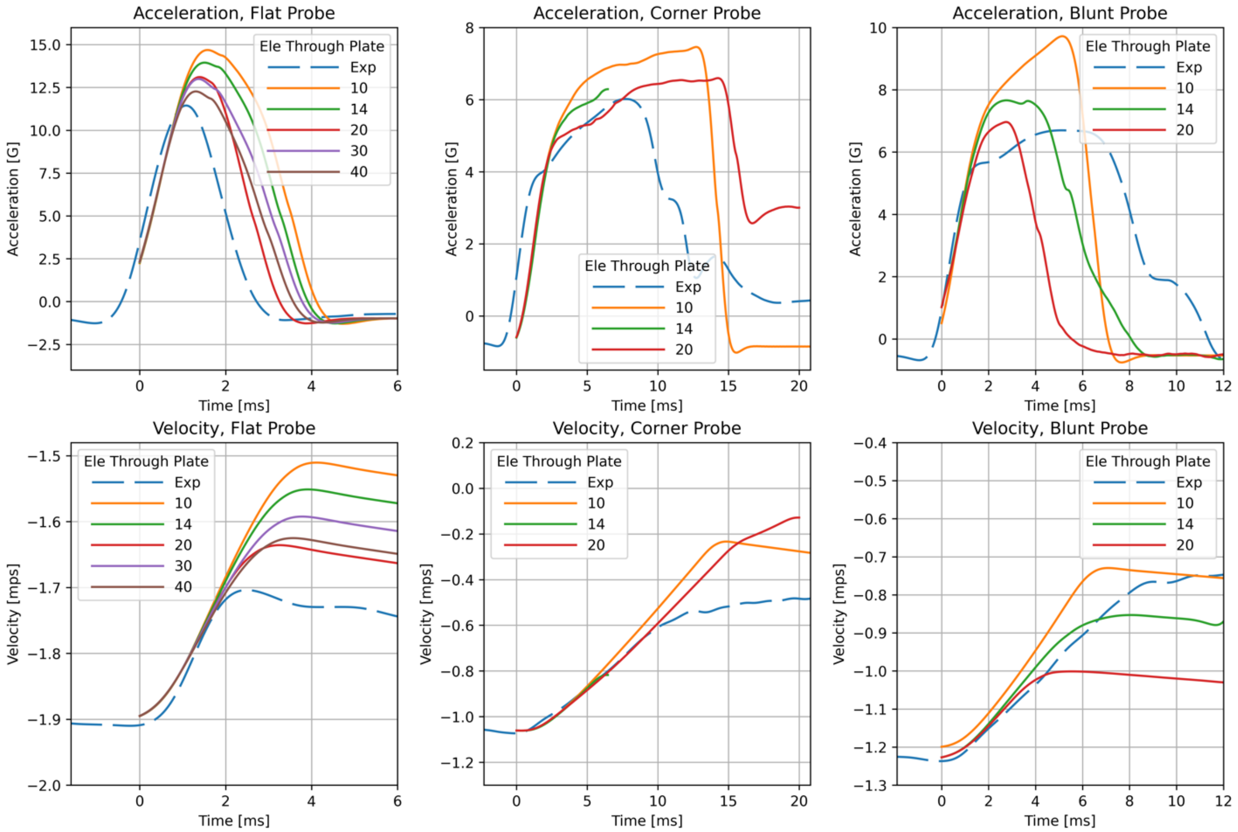

Figure 22. Acceleration and velocity time histories are plotted for plates of thickness 0.114 inch comparing varying number of elements through the plate thickness

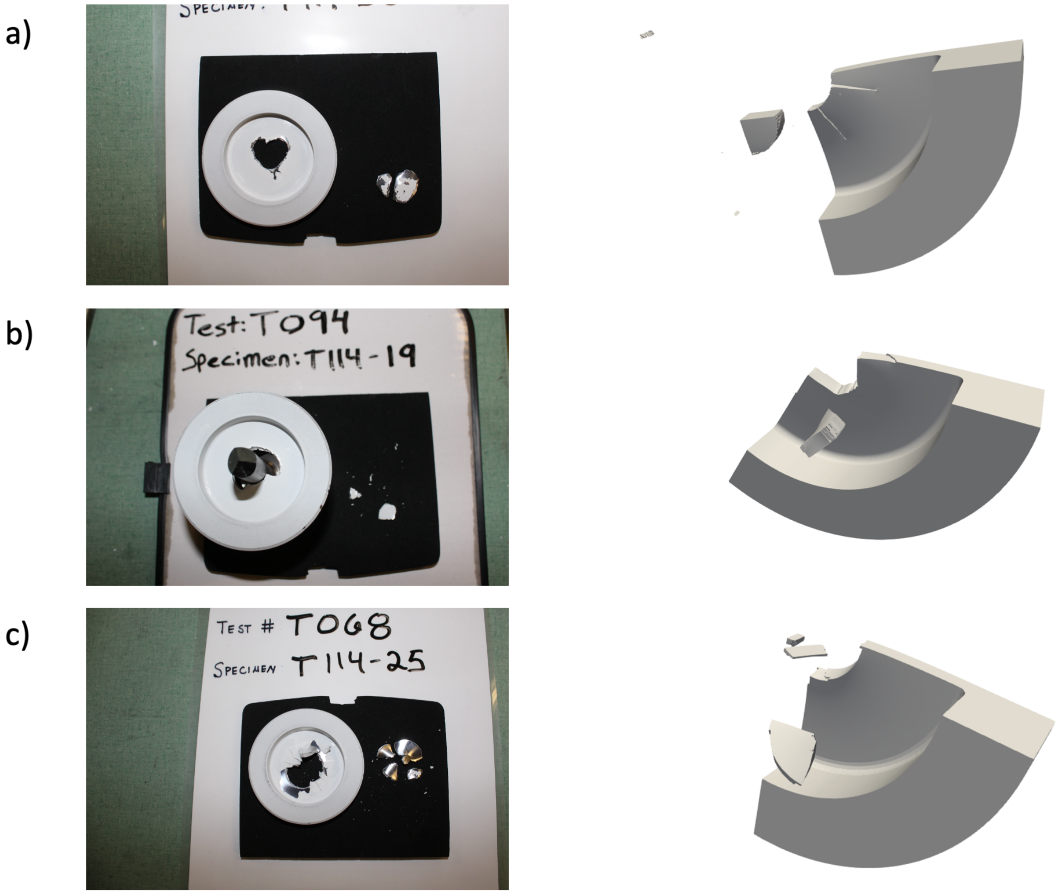

Figure 23. A qualitative comparison is made between 0.114 inch plates, post-puncture, comparing simulation and experiment. Flat probes are compared in (a), tri-corner probes in (b), and blunt probes in (c)

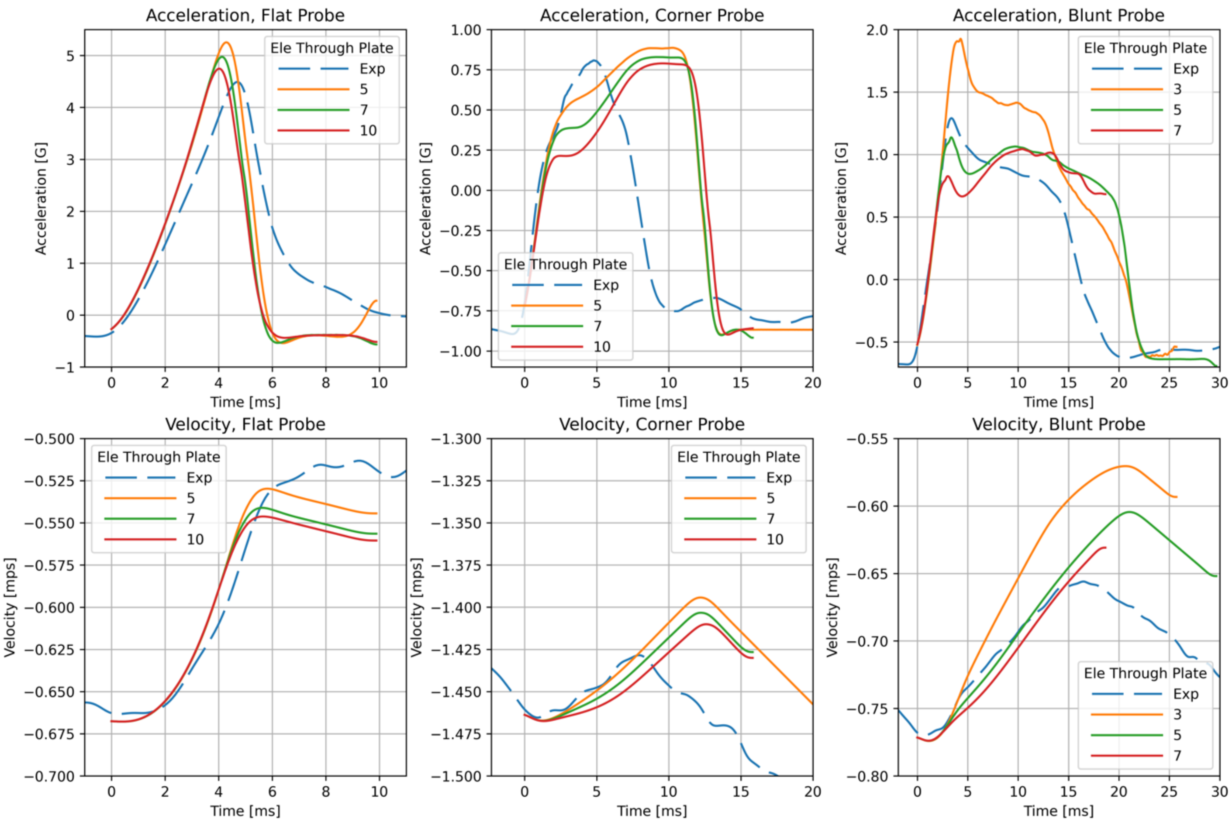

Figure 24. Acceleration and velocity time histories are plotted for plates of thickness 0.051 inch comparing mesh sizes with varying number of elements through the thickness

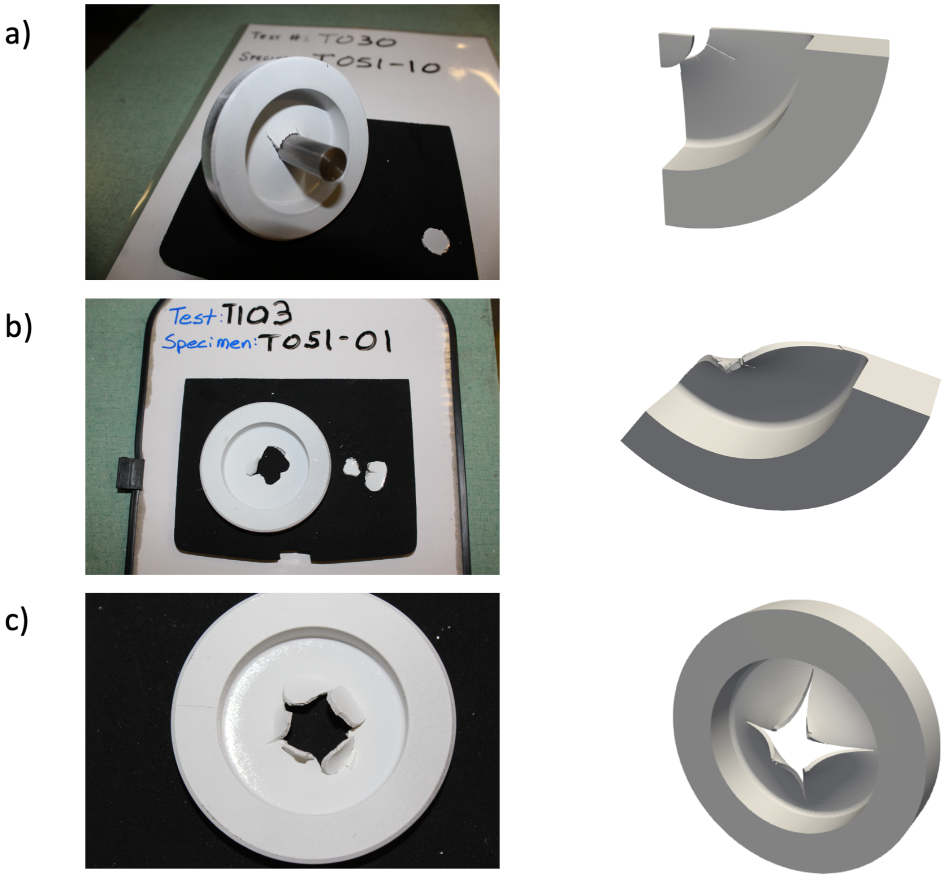

Figure 25. A qualitative comparison is made between 0.051” plates, post-puncture, comparing simulation and experiment. Flat probes are compared in (a), tri-corner probes in (b), and blunt probes in (c)

Table 6. Energy absorbed by the plate is summarized across all mesh studies

Plate Thick. [in.]	**Probe Type**	**Elements Through Thickness**	**Absorbed Energy, Peak Accel [J] (simulation)**	**Absorbed Energy, Peak Accel [J] (experiment)**	**Absorbed Energy, Full Puncture [J] (simulation)**	**Absorbed Energy, Full Puncture [J] (experiment)**
0.250	Flat	10	112	66	232	167
		14	110		231	
		20	106		229	
		30	100		187	
		40	100		171	
	Tri-Corner	10	194	129	350	292
		14	167		339	
		20	127		284	
	Blunt	10	248	66	382	254
		14	110		233	
		20	108		213	
0.114	Flat	10	40	25	100	59
		14	39		91	
		20	33		71	
		30	33		82	
		40	28		74	
	Tri-Corner	5	78	50	89	78
		7	77		89	
		10	81		84	
		14	DNF		DNF	
		20	82		DNF	
	Blunt	7	69	48	82	75
		10	54		67	
		14	27		60	
		20	24		40	
0.051	Flat	5	9	9	13	15
		7	9		13	
		10	8		12	
	Tri-Corner	5	32	11	36	20
		7	31		34	
		10	29		34	
	Blunt	3	5	3	36	17
		5	3		23	
		7	2		DNF	

Across all cases, clean mesh convergence trends are not generally observed. This is perhaps expected: with smaller elements the “crack” formed through element death becomes increasingly sharp facilitating an easier failure. As such, convergent results should only be expected up to the point of failure initiation. However, these mesh studies seek to convey the sensitivity inherent across mesh sizes spanning a “reasonable number of elements”. Based on prior work, a reasonable number is in the neighborhood of 20 elements through the thickness of the 0.250” plate and 5 elements through the 0.051” plate. In practice, mesh size is limited by acceptable computational expense which for present purposes does not exceed a 50-hour run.

Simulation results are arguably best aligned for the thickest plates (0.250”) as seen in Figure 20. Here, across all probe types, the peak acceleration is well approximated within the tested mesh sizes. For the blunt and corner tip probes, 20 elements through the thickness appears adequate. In contrast, the flat probe, perhaps owing to sharp gradients formed at the circumference of the probe, needs closer to 40 elements through the thickness. Qualitatively, the simulations correctly predict plugs being severed from the plate as the probe passes through. This is seen in Figure 21.

Results for plates with a thickness of 0.114” are notably less aligned. Part of this may be attributed to inadequate mesh refinement: both flat and corner probe responses are overpredicted as seen in Figure 22. Based on observable trends, one would expect that further mesh refinement would better align these results. However, the computational expense quickly becomes prohibitive. To this point, several simulations did not finish (DNF). These were terminated on time. For the blunt probe, the impulse shape is wholly missed resulting in substantial error. Despite this, the qualitative behavior is reasonably predicted with the simulation correctly predicting four separated pieces as in Figure 23c.

For the 0.051” plates, the largest error is seen with the tri-corner probe where again the shape of the impulse is missed as seen in Figure 24. For this case, the simulation predicts that the probe tears through the plate as opposed to severing a plug. Experimentally, this is clearly not the case. See Figure 25b as evidence.

Regarding predictions for absorbed energy, predictions show moderate mesh sensitivity with variations on the order of 50% across mesh sizes. An error assessment, comparing nominal mesh sizes to experiment, is deferred to a later section.

Puncture Results with 1.0” Diameter Punch

In the above section, mesh studies were conducted for probes having a diameter of 0.5 inches. Further experiments were conducted using a larger probe diameter of 1.0 inches. These are also simulated. However, instead of conducting additional mesh studies, the nominal mesh sizes from the existing studies, using the 0.5” diameter probes, are used. For each case, this is the mesh size that achieves reasonable agreement with experiment while balancing computational cost. Mesh sizes for these runs are tabulated in Table 7.

Table 7. The mesh size, in terms of elements though plate thickness, is summarized for simulations using a 1.0” punch

	Flat	**Tri-Corner**	**Blunt**
0.250	40	20	20
0.114	20	14	14
0.051	5	5	5

Results are presented in the same fashion as before, with time histories for each plate thickness included in Figure 26, Figure 27, and Figure 28 respectively. Work to failure is summarized in Table 8.

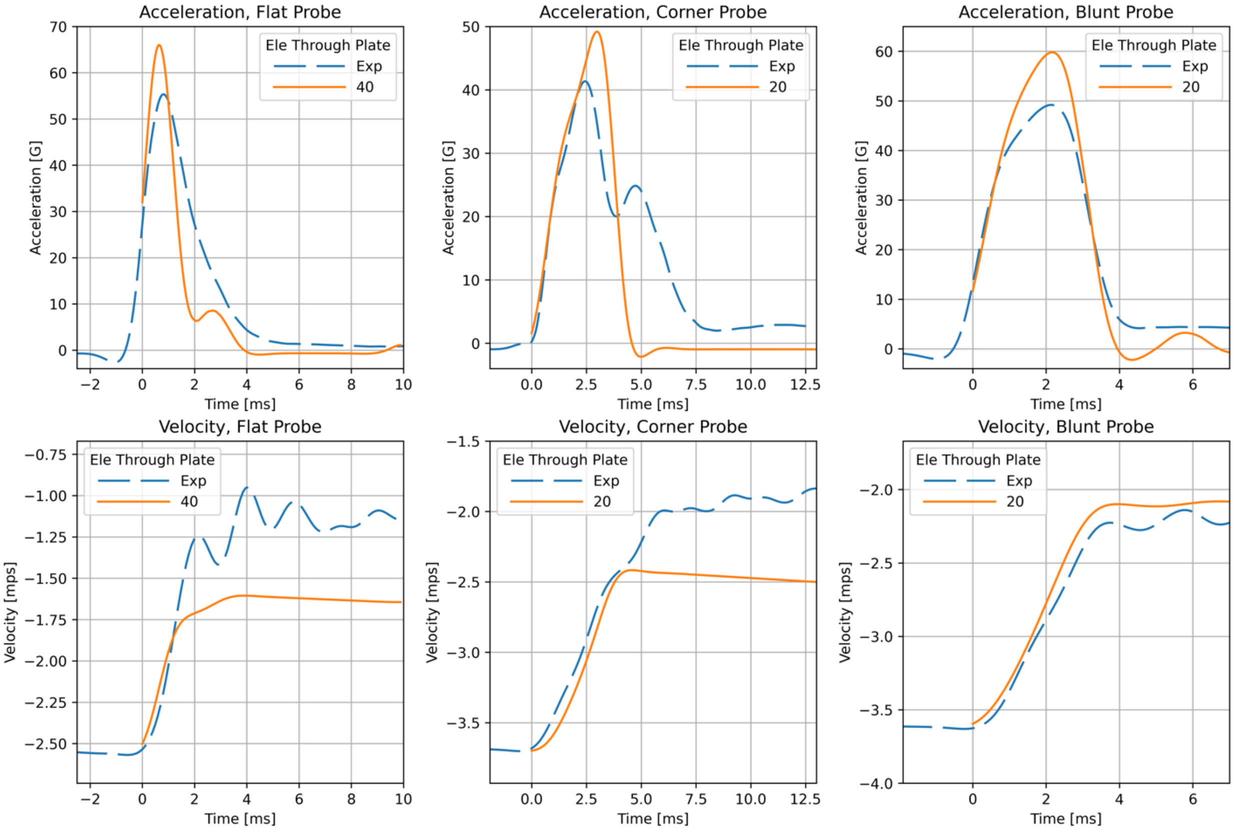

Figure 26. Acceleration and velocity time histories are plotted for all simulations using a 1.0 inch dimeter probe and plate thickness of 0.250 inch.

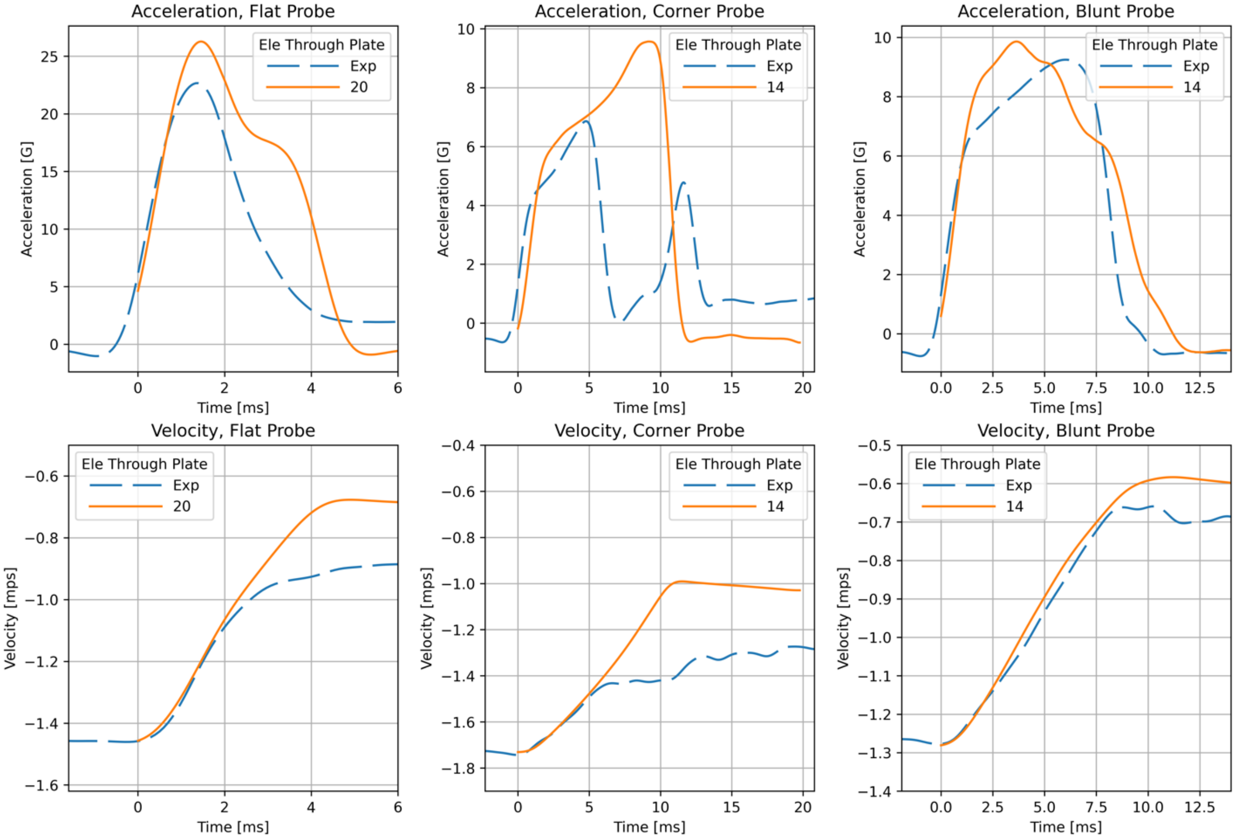

Figure 27. Acceleration and velocity time histories are plotted for all simulations using a 1.0 inch dimeter probe and plate thickness of 0.114 inch.

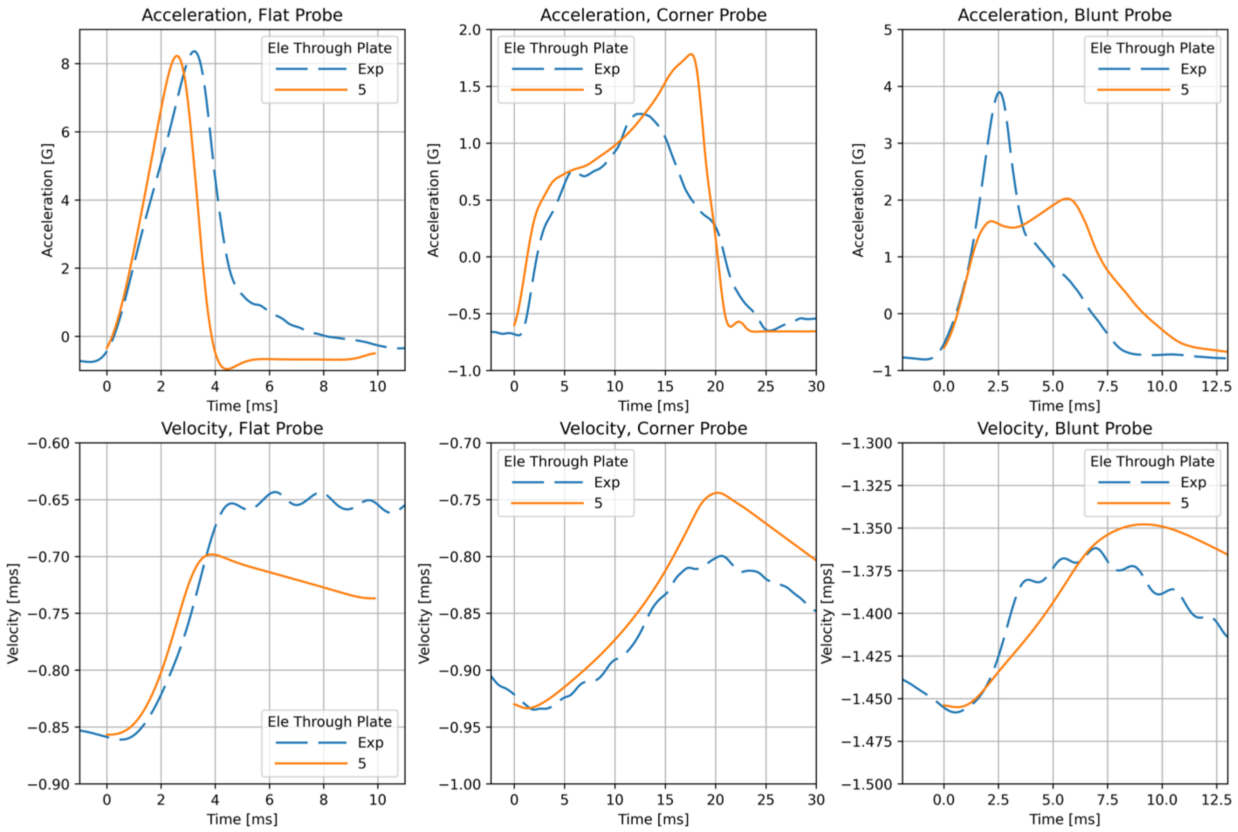

Figure 28. Acceleration and velocity time histories are plotted for all simulations using a 1.0 inch dimeter probe and plate thickness of 0.051inch.

Table 8. Work-to-failure results are summarized for all simulations with a 1 inch diameter probe

Plate Thick. [in.]	**Probe Type**	**Elements Through Thickness**	**Absorbed Energy, Peak Accel [J] (simulation)**	**Absorbed Energy, Peak Accel [J] (experiment)**	**Absorbed Energy [J] (simulation)**	**Absorbed Energy [J] (experiment)**
0.250	Flat	40	109	146	268	384
	Tri-Corner	20	418	365	571	725
	Blunt	20	414	381	617	590
0.114	Flat	20	52	42	121	99
	Tri-Corner	14	134	60	154	77
	Blunt	14	45	71	100	91
0.051	Flat	5	12	15	25	28
	Tri-Corner	5	33	17	38	33
	Blunt	5	23	10	36	29

Transitioning from the 0.5” probe to the 1.0” probe, results seem reasonably aligned. Qualitatively, acceleration pulse shapes are generally predicted with a noteworthy exception being the corner probe on the 0.114” plate. Experimentally, the acceleration profile for this case shows a dual peak shape. This is one scenario in which the “end” of the impulse is not well defined. However, based on repeat experiments plotted in Figure 29, the end of the impulse is taken at the base of the first peak. This plot illustrates that uncertainty exists on the experimental end in addition to the simulations.

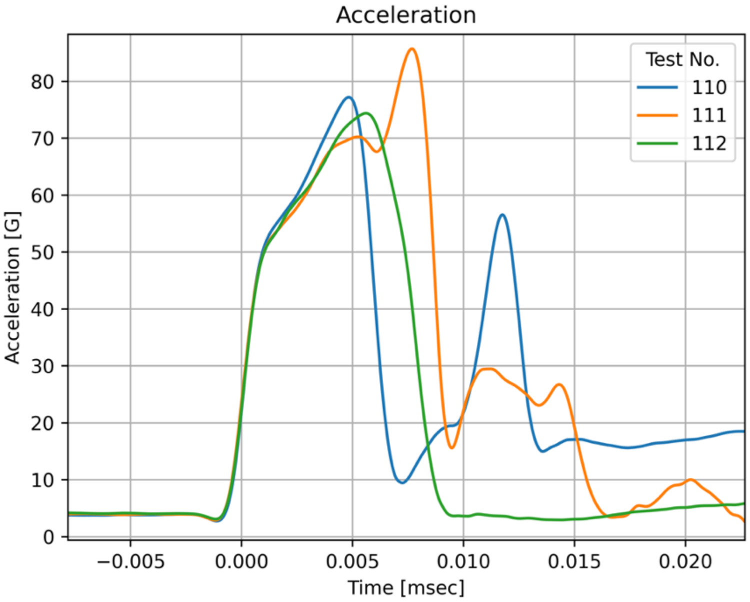

Figure 29. Accleration pulses are plotted for three repeat experiments all run with the same probe and plate. For these tests, the probe is a tri-corner with diameter 1.0". The plate has a thickness of 0.114 inch.

Puncture Results for 0.25” Diameter Probe

For only the flat probe shape, further experiments where run using a probe with a diameter of 0.25 inches. As before, the “ideal” mesh size is assumed from the mesh studies performed with the 0.5” probes as in Table 7. Results are organized somewhat differently owing to the single probe shape involved. Acceleration and velocity time histories are plotted for all plate thicknesses in Figure 30. Work-to-failure results are summarized in Table 9.

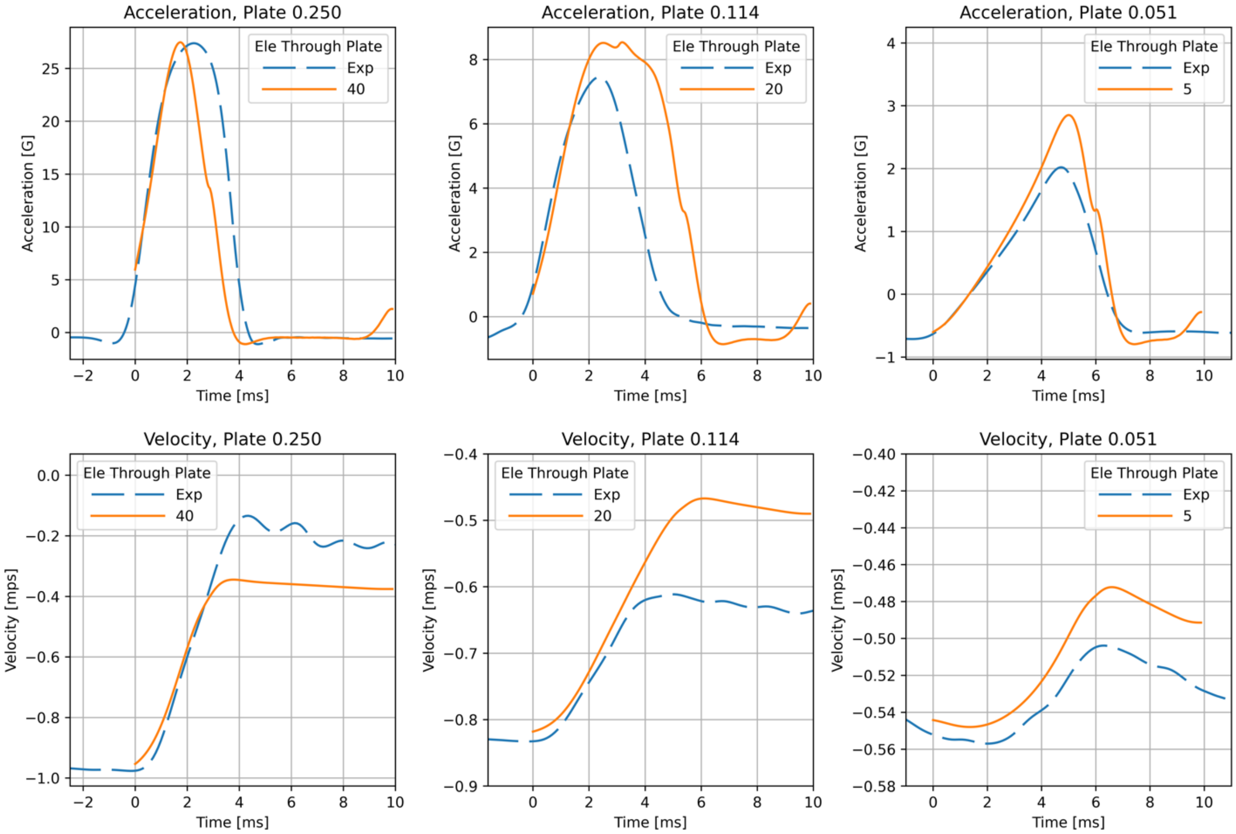

Figure 30. Acceleration and velocity time histories are plotted for flat probes with diameter 0.25 inch.

Table 9. Work-to-failure is summarized for flat probes with diameter 0.25 inch.

Plate Thickness [inches]	Probe Type	Elements Through Thickness	Absorbed Energy, Peak Accel [J] (simulation)	Absorbed Energy, Peak Accel [J] (experiment)	Absorbed Energy [J] (simulation)	Absorbed Energy [J] (experiment)
0.250	Flat	40	35	49	57	68
0.114	Flat	20	19	15	36	27
0.051	Flat	5	6	5	9	7

Across the three probe shapes, flat probes generally show the best agreement. With the 0.25” punches, agreement remains reasonable: the acceleration pulse is well captured with differences that might easily attribute to mesh refinement. Likewise, absorbed energy is predicted to within 35% across all cases.

Error Summary

A visual presentation of error, comparing absorbed energy predictions with experiment, is provided in Figure 31. Errors are binned according to both probe type (left) and plate thickness (right). Differentiation is made between energy absorbed up to the peak-acceleration and energy absorbed over the full puncture event. Several noteworthy trends are observed. First off, the simulations more reliably predict absorbed energy over the full puncture event as compared to absorbed energy up to only the peak acceleration. This is contrary to what was initially expected considering mesh sensitivity to crack propagation. However, the peak acceleration may not be a good point of comparison between simulation and experiment. This is especially the case when the simulation predicts a different impulse shape compared to experiment. An obvious example is the corner probe in Figure 27. Generally, the impulse shape is better predicted for flat probes. Hence it comes as no surprise that predictions for absorbed energy, up to peak acceleration, are best for this probe shape.

In contrast, absorbed energy over the whole puncture event is a far more stable metric for comparison. Considering these values, errors are within ± 50% across all cases. As regards plate thickness, predictions are more reliable for the thickest plate (0.250") and worst for the middle thickness plate (0.114"). This might partially be attributed to inadequate mesh refinement for the 0.114" plates. Recall further refinement becomes computationally intractable.

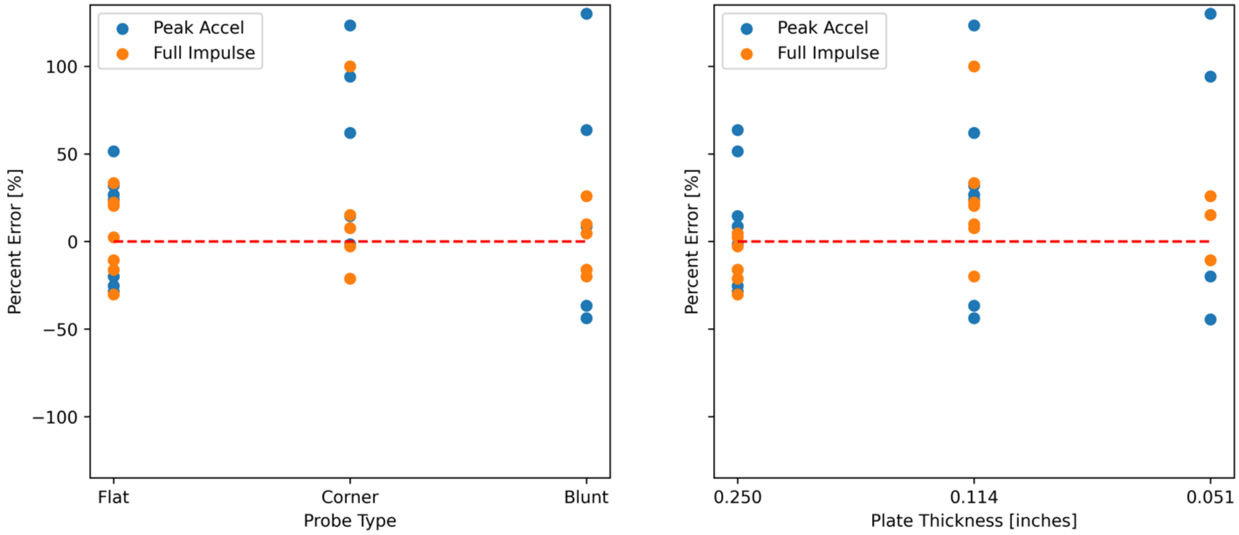

Figure 31. The percent error of predicted energy absorbtion is summarized according to probe type (left) and plate thickness (right). Predictions are included for energy absorbed up to peak acceleration and for energy absorbed over the whole puncture event.

Conclusion

The question of how well the calibration performs is partially obscured by mesh sensitivity. This problem is complicated by the inability to further refine the mesh in instances were doing so would likely better align results. Within the array of current results, absorbed energy, calculated over the full puncture, is predicted to within 50% for all but one outlier. In contrast, energy absorbed up to the peak acceleration is more variable with some errors in excess of 100%. Larger errors in this metric may indicate that the peak acceleration is not a good reference for comparison, particularly when the impulse shape is not well captured. See for example the corner probe in Figure 28 where the experimental and simulated peak accelerations are separated by 5ms. The end of the impulse, however, is a more reliable reference for comparison.

On the topic of outliers, the calibration does fail to correctly predict the mode of failure in some specific cases. A good example of this would be the 0.5” diameter corner probe on the thinnest plate of 0.051 inches. Here, it is quite obvious that in reality the probe punches out material as seen in Figure 25b. However, in simulation, the plate is “torn” up to the point where the probe can pass through without separating a plug. As a result, the predicted absorbed energy shows sizable error. More generally, the theme of overly preferencing this tearing mode is hinted at across several cases. See for instance the flat probe with a plate of 0.114 inches in Figure 23a. Cracks can be seen extending radially outward in simulation with no such features present experimentally.

To summarize, absorbed energy, over the full puncture, is predicted to within 50% excepting one outlier. This metric is preferred over absorbed energy up to the peak failure which shows a larger spread. Not surprisingly, error is largest for those cases where the impulse shape is poorly predicted. In some instances, this occurs because the simulation predicts a different tearing behavior compared to reality. For those cases where the general impulse shape is captured, errors are closer to 30%.

Acknowledgments

The material testing was conducted in the Structural Mechanics Laboratory by Pat Carrion. Puncture tests were conducted in the Component Mechanical Shock Laboratory by Dylan Landry. Their contributions are acknowledged with thanks.

Sandia National Laboratories is a multimission laboratory managed and operated by National Technology and Engineering Solutions of Sandia, LLC, a wholly owned subsidiary of Honeywell International Inc., for the U.S. Department of Energy's National Nuclear Security Administration under contract DE-NA0003525.

References

[1] LAMÉ team. Library of Advanced Materials for Engineering (LAMÉ) 5.4, SAND 2021-16079, December 2022

[2] Corona, E., Spletzer, Lester, B., Fietek, C. *Validation of material models for puncture of 7075-T651 aluminum plate*, International Journal of Solids and Structures, Volume 257, 2022, 111893, ISSN 0020-7683, https://doi.org/10.1016/j.ijsolstr.2022.111893.

[3] Wilkins, M L, Streit, R D, and Reaugh, J E. *Cumulative-strain-damage model of ductile fracture: simulation and prediction of engineering fracture tests*. United States: N. p., 1980. Web. doi:10.2172/6628920.

Appendix

A: Updated Hill Yield Surface

A correction is introduced to the material model used in the above report. Specifically, the Hill anisotropic yield surface is adjusted to better fit the tensile behavior for the “transverse” direction. Recall the flow stress is lower for this orientation as seen in Figure 1. Compared to the calibration in the report, the Hill constants R11, R22, and R12 are adjusted to 0.86 where they were originally 1.0. This is the only change.

The influence of this edit is most visible in Figure 32 which plots both simulation and experimental curves for tension in both the axial and transverse orientations. Comparison is made between earlier predictions and those using the updated Hill constants. Prior to the update, both the transverse and axial orientations look nearly identical. However, with the updated yield surface the flow stress in the transverse orientation is reduced better matching experiment.

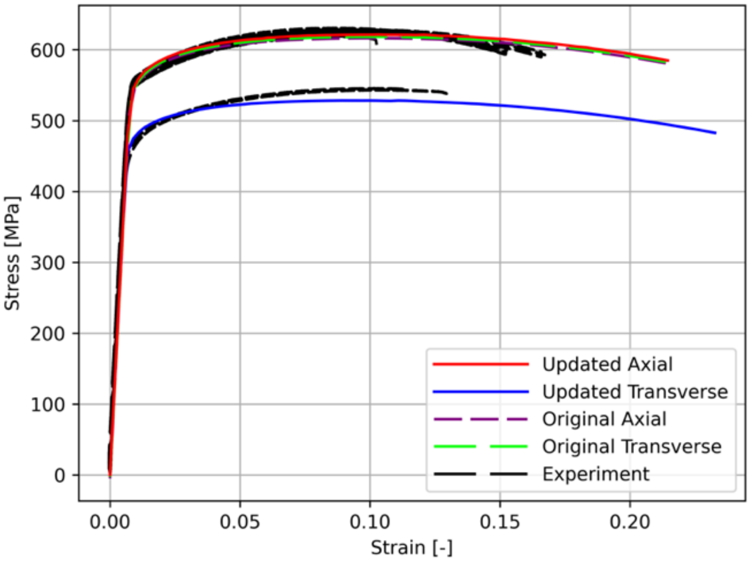

Figure 32. Stress-strain is plotted for tension tests in both the axial and transverse orientations. Predictions are plotted for both the original and updated yield surface.

With this update, several pertinent results from the report are recreated. First, plots presented in the “Calibration Summary” section are redeveloped using the revised yield surface. The same format is followed as before with tension, notch, hat, and rate results presented in Figures Figure **33**-Figure **36** respectively. Comparison to earlier results, in the main body of the report, shows limited influence of the updated yield surface.

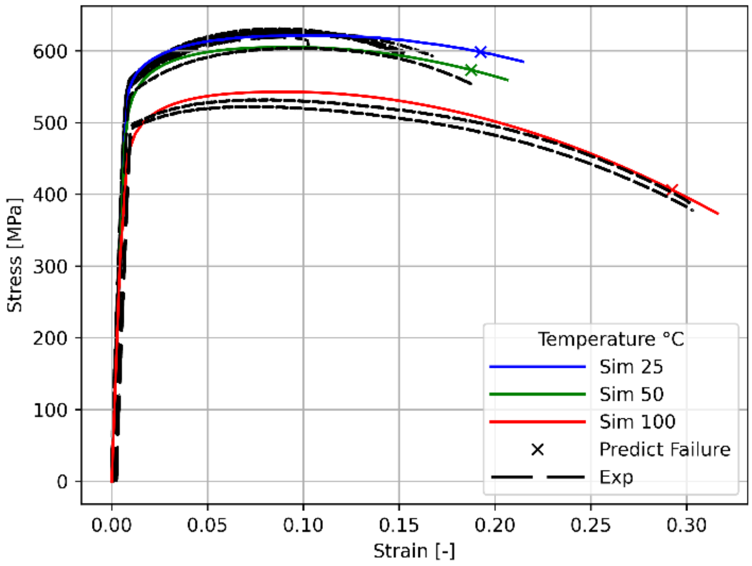

Figure 33. Tension results for varying temperature are recreated with the updated yield surface. Simulation results are plotted atop experimental curves.

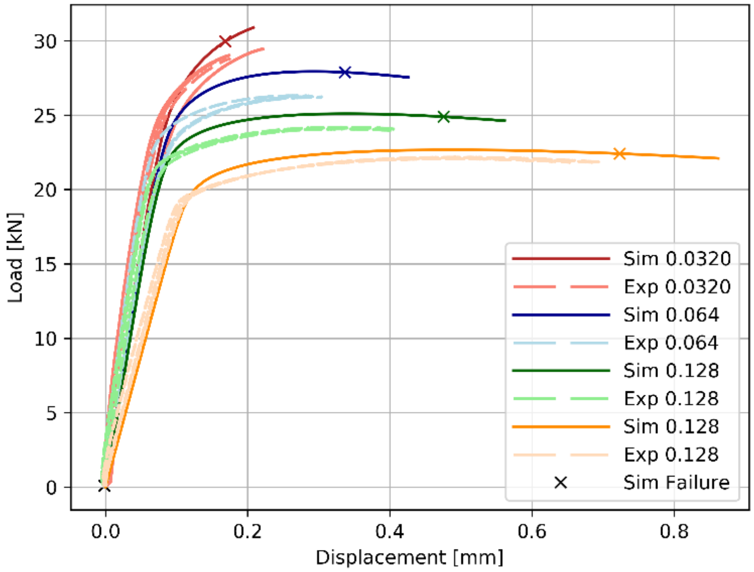

Figure 34. Notch results are rerun with the updated yield surface and plotted with experiment

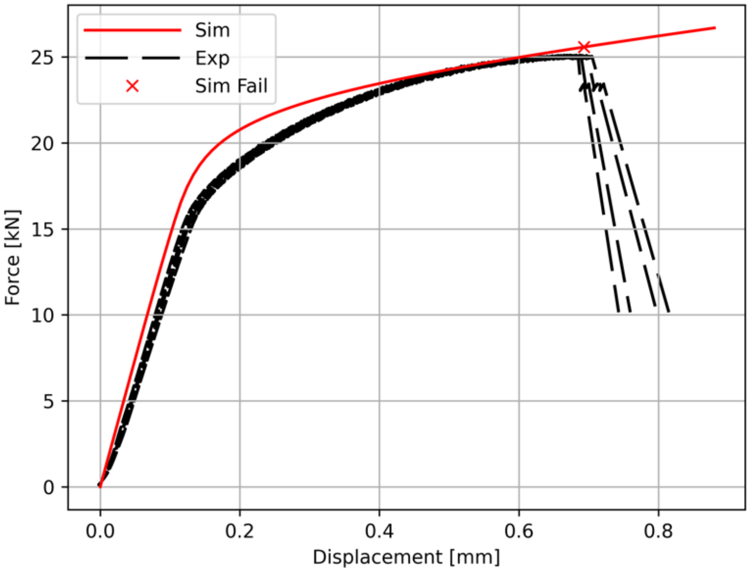

Figure 35. Hat compression is rerun with the updated yield surface and results plotted alongside experiment

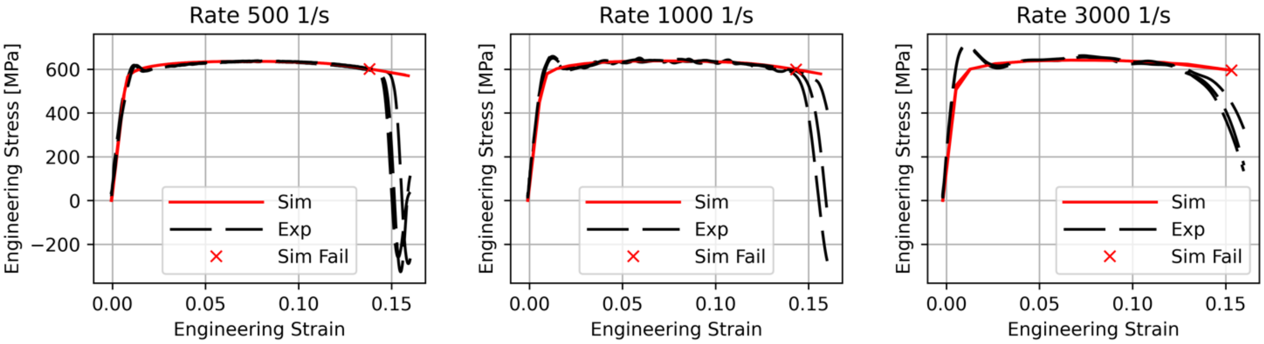

Figure 36. High-rate tests are resimulated with the updated yield surface and plotted against experiment

In addition to the above calibration simulations, select puncture simulations for the flat probe with diameter 0.5” are rerun across all plate thicknesses. For each, only the “nominal” mesh size, as determined in the mesh studies, is simulated. These results are presented in Figure 37. Work-to-failure metrics are compared in **Table 10**.

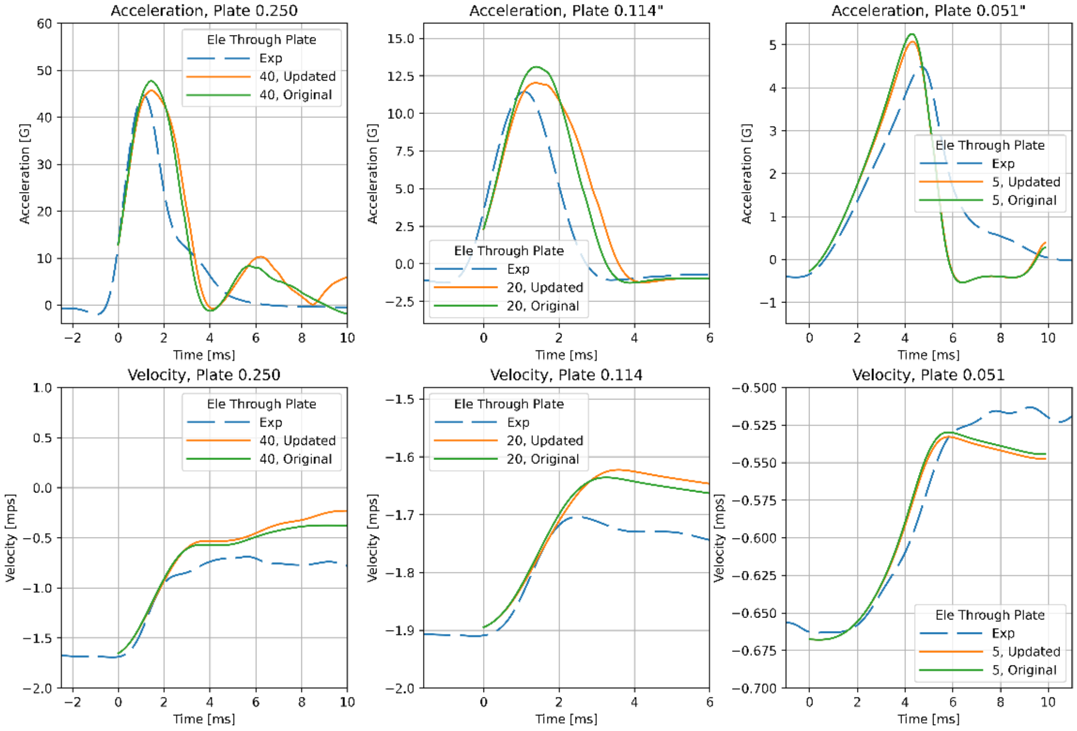

Figure 37. Puncture results for the flat probe with a diameter of 0.5" are rerun with the updated yield surface. New predictions are plotted alongside the earlier predictions with experimental curves also shown.

Table 10. Absorbed energy is tabulated for puncture simulations and experiment. Simulation results for both the original and updated yield surface are included

Plate Thickness [inches]	Probe Type	Elements Through Thickness	Absorbed Energy Over Full Puncture [J] (simulation)		Absorbed Energy Over Full Puncture [J] (experiment)
			Updated	**Original**	
0.250	Flat	40	174	171	167
0.114	Flat	20	74	71	59
0.051	Flat	5	13	13	15

For the above results, the modification to the Hill yield surface shows marginal impact. Comparing the work-to-failure between the original and updated results, differences are on the order of 4%. This is negligible when compared to mesh uncertainty and other error sources.

B: Specimen Drawings

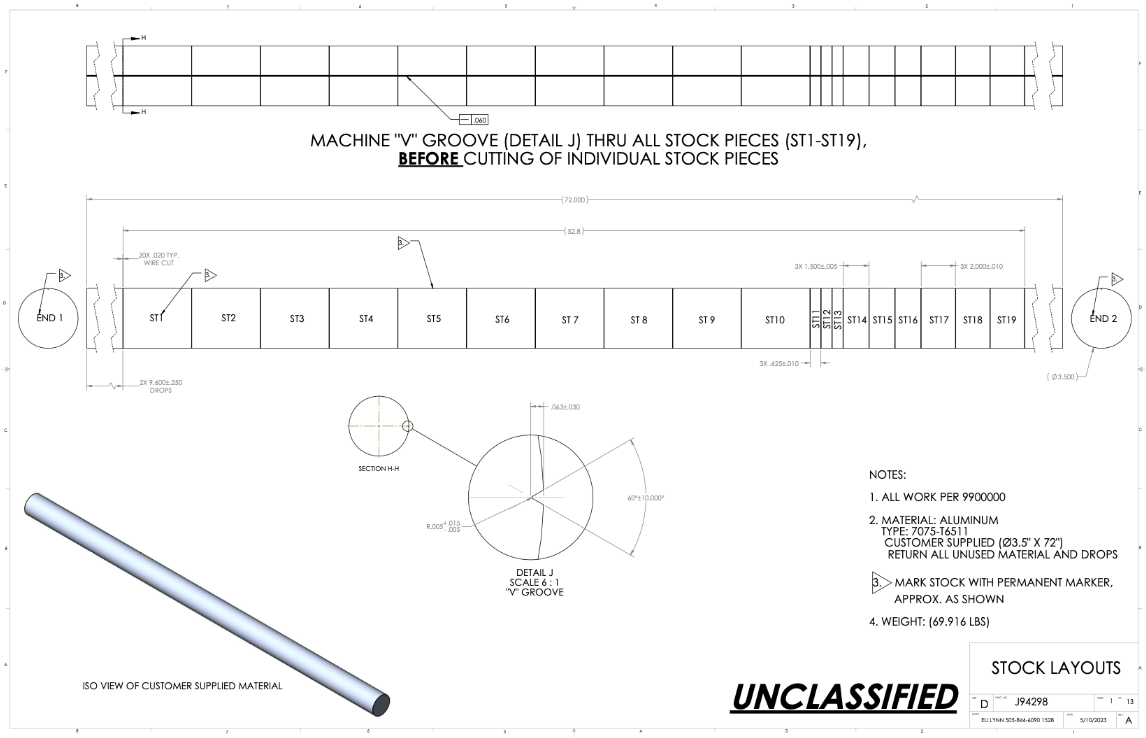

NOTES:

1. ALL WORK PER 9900000
2. MATERIAL: ALUMINUM
   TYPE: 7075-T6511
   CUSTOMER SUPPLIED (Ø3.5" X 72")
   RETURN ALL UNUSED MATERIAL AND DROPS
3. MARK STOCK WITH PERMANENT MARKER, APPROX. AS SHOWN
4. WEIGHT: (69.916 LBS)

UNCLASSIFIED

STOCK LAYOUTS
D J94298 1 13
ELI LYNN 505-844-6090 1528 5/10/2023 A

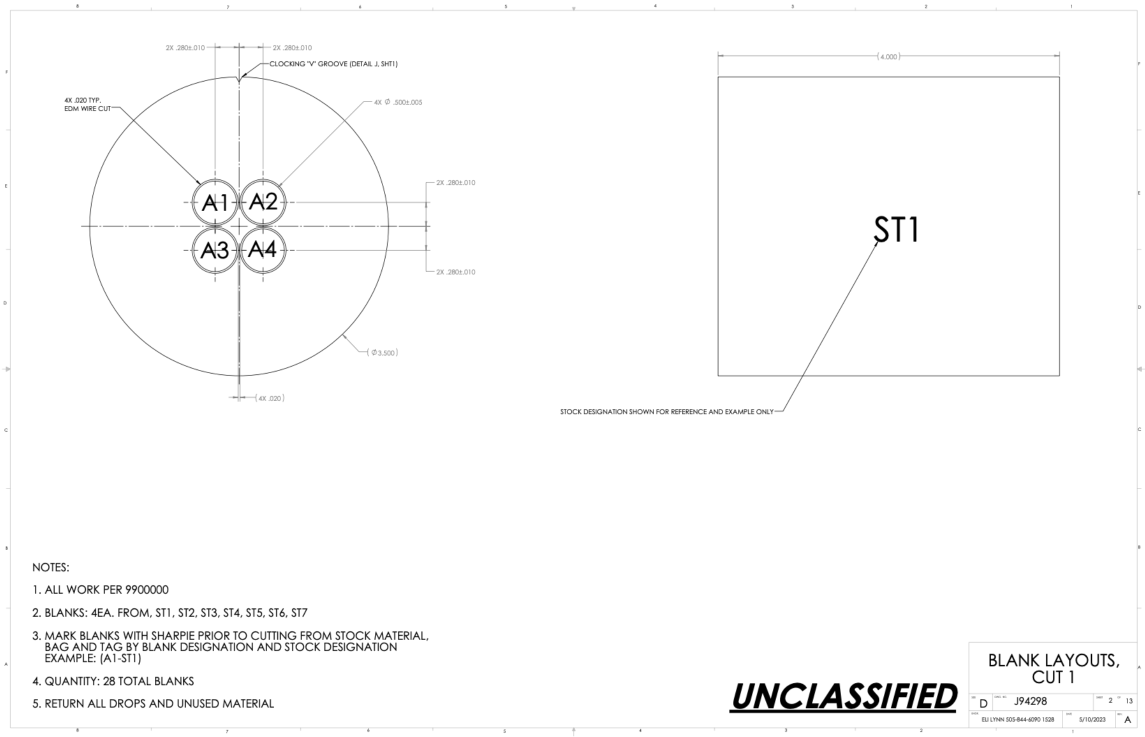

NOTES:

1. ALL WORK PER 9900000
2. BLANKS: 4EA. FROM, ST1, ST2, ST3, ST4, ST5, ST6, ST7
3. MARK BLANKS WITH SHARPIE PRIOR TO CUTTING FROM STOCK MATERIAL, BAG AND TAG BY BLANK DESIGNATION AND STOCK DESIGNATION EXAMPLE: (A1-ST1)
4. QUANTITY: 28 TOTAL BLANKS
5. RETURN ALL DROPS AND UNUSED MATERIAL

UNCLASSIFIED

BLANK LAYOUTS,
CUT 1
D J94298 2 13
ELI LYNN 505-844-6090 1528 5/10/2023 A

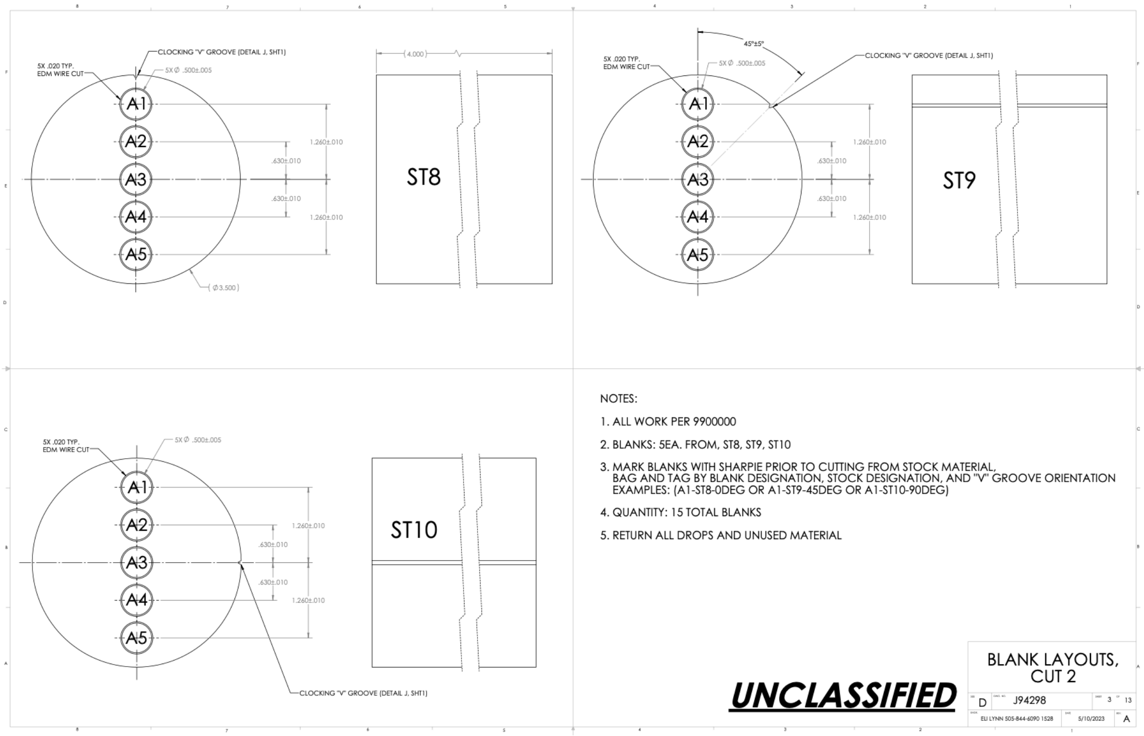

NOTES:

1. ALL WORK PER 9900000
2. BLANKS: 5EA. FROM, ST8, ST9, ST10
3. MARK BLANKS WITH SHARPIE PRIOR TO CUTTING FROM STOCK MATERIAL, BAG AND TAG BY BLANK DESIGNATION, STOCK DESIGNATION, AND "V" GROOVE ORIENTATION EXAMPLES: (A1-ST8-0DEG OR A1-ST9-45DEG OR A1-ST10-90DEG)
4. QUANTITY: 15 TOTAL BLANKS
5. RETURN ALL DROPS AND UNUSED MATERIAL

UNCLASSIFIED

BLANK LAYOUTS,
CUT 2

D	J94298	3	13
ELI LYNN 505-844-6090 1528	5/10/2023	A	

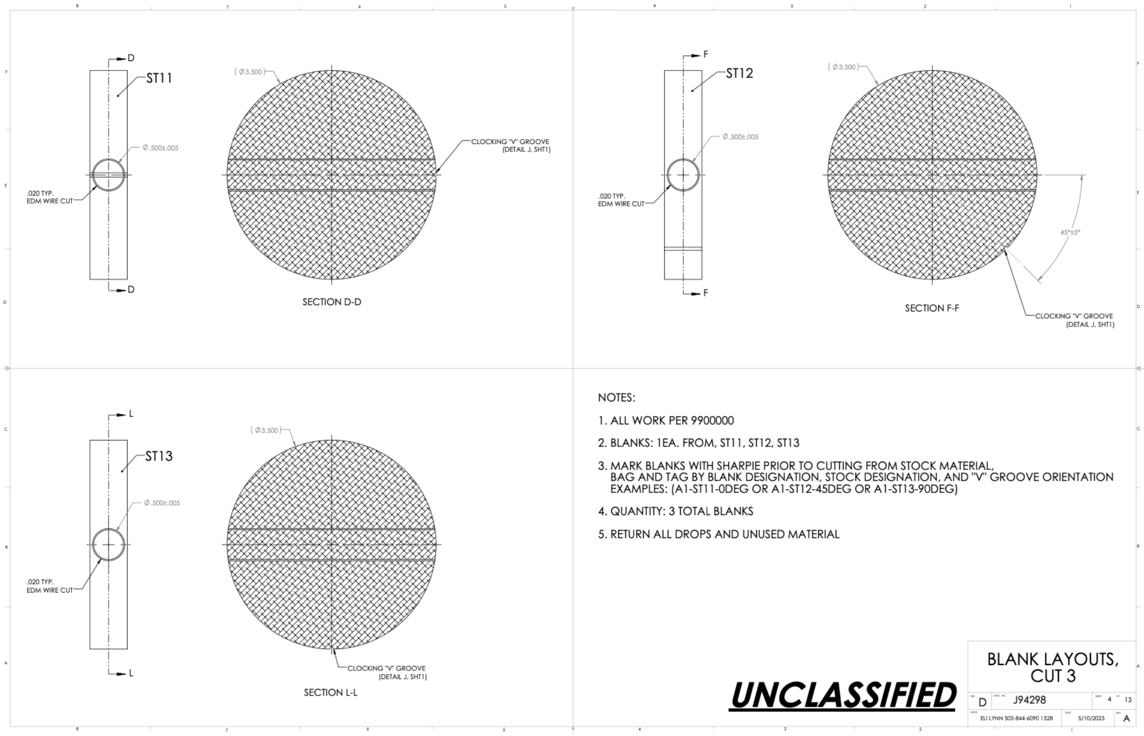

NOTES:

1. ALL WORK PER 9900000
2. BLANKS: 1EA. FROM, ST11, ST12, ST13
3. MARK BLANKS WITH SHARPIE PRIOR TO CUTTING FROM STOCK MATERIAL, BAG AND TAG BY BLANK DESIGNATION, STOCK DESIGNATION, AND "V" GROOVE ORIENTATION EXAMPLES: (A1-ST11-0DEG OR A1-ST12-45DEG OR A1-ST13-90DEG)
4. QUANTITY: 3 TOTAL BLANKS
5. RETURN ALL DROPS AND UNUSED MATERIAL

UNCLASSIFIED

BLANK LAYOUTS,
CUT 3

D	J94298	4	13
ELI LYNN 505-844-6090 1528	5/10/2023	A	

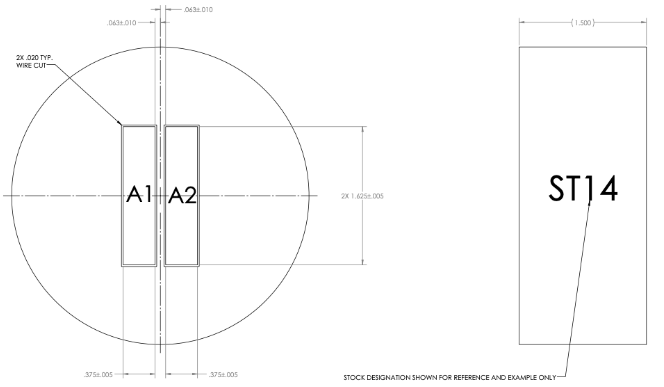

NOTES:

1. ALL WORK PER 9900000
2. MATERIAL: 2EA. FROM, ST14, ST15, ST16
3. MARK BLANKS WITH SHARPIE PRIOR TO CUTTING FROM STOCK MATERIAL, BAG AND TAG BY BLANK DESIGNATION AND STOCK DESIGNATION EXAMPLE: (A1-ST14)
4. QUANTITY: 6 TOTAL BLANKS
5. RETURN ALL DROPS AND UNUSED MATERIAL

UNCLASSIFIED

BLANK LAYOUTS,
CUT 4
D J94298 5 13
ELI LYNN 505-844-6090 1528 5/10/2023 A

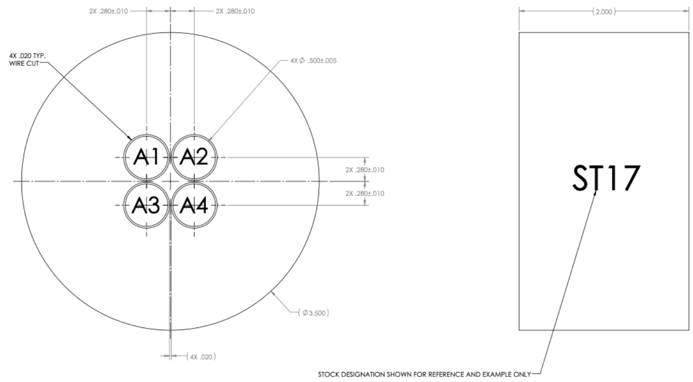

NOTES:

1. ALL WORK PER 9900000
2. MATERIAL: 4EA. FROM, ST17, ST18, ST19
3. MARK BLANKS WITH SHARPIE PRIOR TO CUTTING FROM STOCK MATERIAL, BAG AND TAG BY BLANK DESIGNATION AND STOCK DESIGNATION EXAMPLE: (A1-ST17)
4. QUANTITY: 12 TOTAL BLANKS
5. RETURN ALL DROPS AND UNUSED MATERIAL

UNCLASSIFIED

BLANK LAYOUTS,
CUT 5
D J94298 6 13
ELI LYNN 505-844-6090 1528 5/10/2023 A

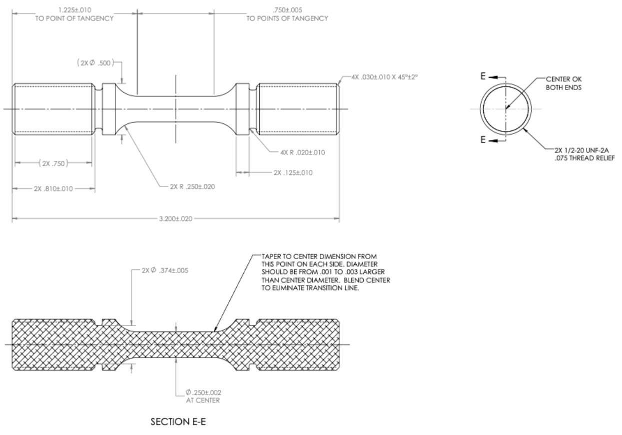

PART NUMBER	MAKE FROM BLANK
J94299-001	A1-ST1
J94299-002	A2-ST1
J94299-003	A3-ST1
J94299-004	A4-ST1
J94299-005	A1-ST2
J94299-006	A2-ST2
J94299-007	A3-ST2
J94299-008	A4-ST2
J94299-009	A1-ST3
J94299-010	A2-ST3
J94299-011	A3-ST3
J94299-012	A4-ST3
J94299-013	A1-ST8
J94299-014	A2-ST8
J94299-015	A3-ST8
J94299-016	A4-ST8
J94299-017	A5-ST8
J94299-018	A1-ST9
J94299-019	A2-ST9
J94299-020	A3-ST9
J94299-021	A4-ST9
J94299-022	A5-ST9
J94299-023	A1-ST10
J94299-024	A2-ST10
J94299-025	A3-ST10
J94299-026	A4-ST10
J94299-027	A5-ST10
J94299-028	ST11
J94299-029	ST12
J94299-030	ST13

TABLE 1

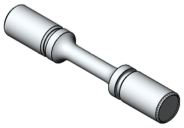

NOTES:

1. ALL WORK PER 9900000

2. MATERIAL: MAKE EACH SPECIMEN USING SPECIFIED BLANK IN TABLE 1.

3. MARK SPECIMENS WITH SHARPIE PER TABLE 1 "PART NUMBER".
BAG AND TAG BY PART NUMBER.
EXAMPLE: (J94299-001)

UNCLASSIFIED

TENSILE SPECIMEN,
Ø.250, 1/2-20 THD
GRIPS

D
J94298
7
13
ELI LYNN 505-844-6090 1528
5/10/2023
A

PART NUMBER	MAKE FROM BLANK
J94300-001	A1-ST4
J94300-002	A2-ST4
J94300-003	A3-ST4
J94300-004	A4-ST4

TABLE 2

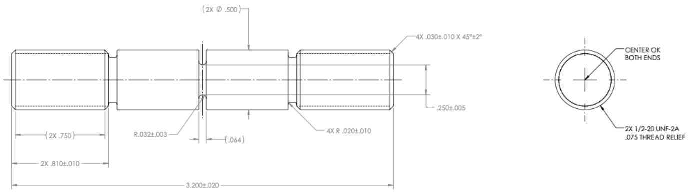

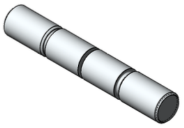

NOTES:

1. ALL WORK PER 9900000

2. MATERIAL: MAKE EACH SPECIMEN USING SPECIFIED BLANK IN TABLE 2.

3. MARK SPECIMENS WITH SHARPIE PER TABLE 2 "PART NUMBER".
BAG AND TAG BY PART NUMBER.
EXAMPLE: (J94300-001)

UNCLASSIFIED

TENSILE SPECIMEN,
R.032, 1/2-20 THD
GRIPS

D
J94298
8
13
ELI LYNN 505-844-6090 1528
5/10/2023
A

PART NUMBER	MAKE FROM BLANK
J94301-001	A1-ST5
J94301-002	A2-ST5
J94301-003	A3-ST5
J94301-004	A4-ST5

TABLE 3

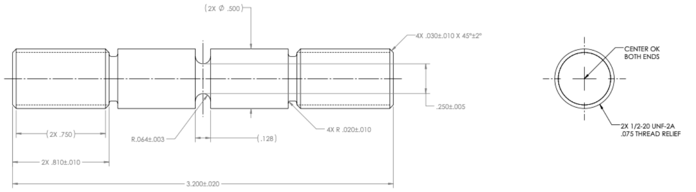

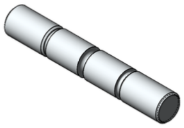

NOTES:

1. ALL WORK PER 9900000
2. MATERIAL: MAKE EACH SPECIMEN USING SPECIFIED BLANK IN TABLE 3.
3. MARK SPECIMENS WITH SHARPIE PER TABLE 3 "PART NUMBER".
   BAG AND TAG BY PART NUMBER.
   EXAMPLE: (J94301-001)

UNCLASSIFIED

TENSILE SPECIMEN,
R.064, 1/2-20 THD
GRIPS

D J94298 9 13

ELI LYNN 505-844-6090 1528 5/10/2023 A

PART NUMBER	MAKE FROM BLANK
J94302-001	A1-ST6
J94302-002	A2-ST6
J94302-003	A3-ST6
J94302-004	A4-ST6

TABLE 4

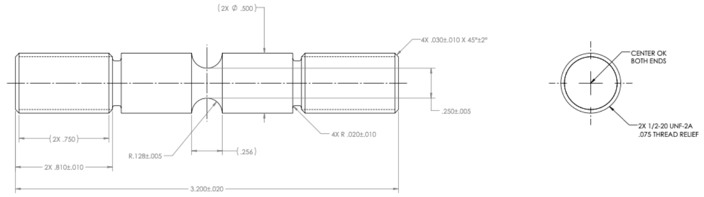

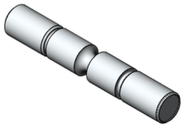

NOTES:

1. ALL WORK PER 9900000
2. MATERIAL: MAKE EACH SPECIMEN USING SPECIFIED BLANK IN TABLE 4.
3. MARK SPECIMENS WITH SHARPIE PER TABLE 4 "PART NUMBER".
   BAG AND TAG BY PART NUMBER.
   EXAMPLE: (J94302-001)

UNCLASSIFIED

TENSILE SPECIMEN,
R.128, 1/2-20 THD
GRIPS

D J94298 10 13

ELI LYNN 505-844-6090 1528 5/10/2023 A

PART NUMBER	MAKE FROM BLANK
J94303-001	A1-ST7
J94303-002	A2-ST7
J94303-003	A3-ST7
J94303-004	A4-ST7

TABLE 5

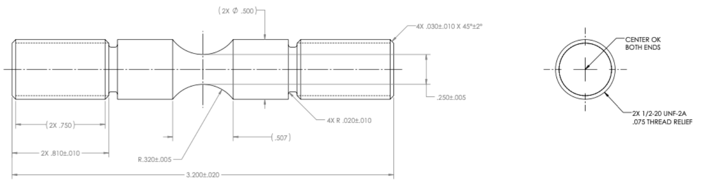

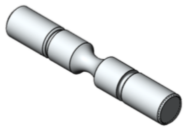

NOTES:

1. ALL WORK PER 9900000
2. MATERIAL: MAKE EACH SPECIMEN USING SPECIFIED BLANK IN TABLE 5.
3. MARK SPECIMENS WITH SHARPIE PER TABLE 5 "PART NUMBER".
   BAG AND TAG BY PART NUMBER.
   EXAMPLE: (J94303-001)

UNCLASSIFIED

TENSILE SPECIMEN,
R.320, 1/2-20 THD
GRIPS
D J94298 11 13
ELI LYNN 505-844-6090 1528 5/10/2023 A

PART NUMBER	MAKE FROM BLANK
J94304-001	A1-ST14
J94304-002	A2-ST14
J94304-003	A1-ST15
J94304-004	A2-ST15
J94304-005	A1-ST16
J94304-006	A2-ST16

TABLE 6

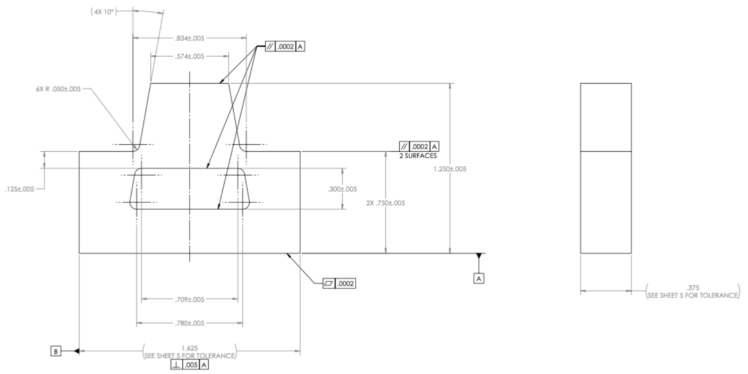

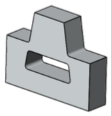

NOTES:

1. ALL WORK PER 9900000
2. MATERIAL: MAKE EACH SPECIMEN USING SPECIFIED BLANK IN TABLE 6.
3. MARK SPECIMENS WITH SHARPIE PER TABLE 6 "PART NUMBER".
   BAG AND TAG BY PART NUMBER.
   EXAMPLE: (J94304-001)

UNCLASSIFIED

LARGE TOP HAT
COMPRESSION
SPECIMEN
D J94298 12 13
ELI LYNN 505-844-6090 1528 5/10/2023 A

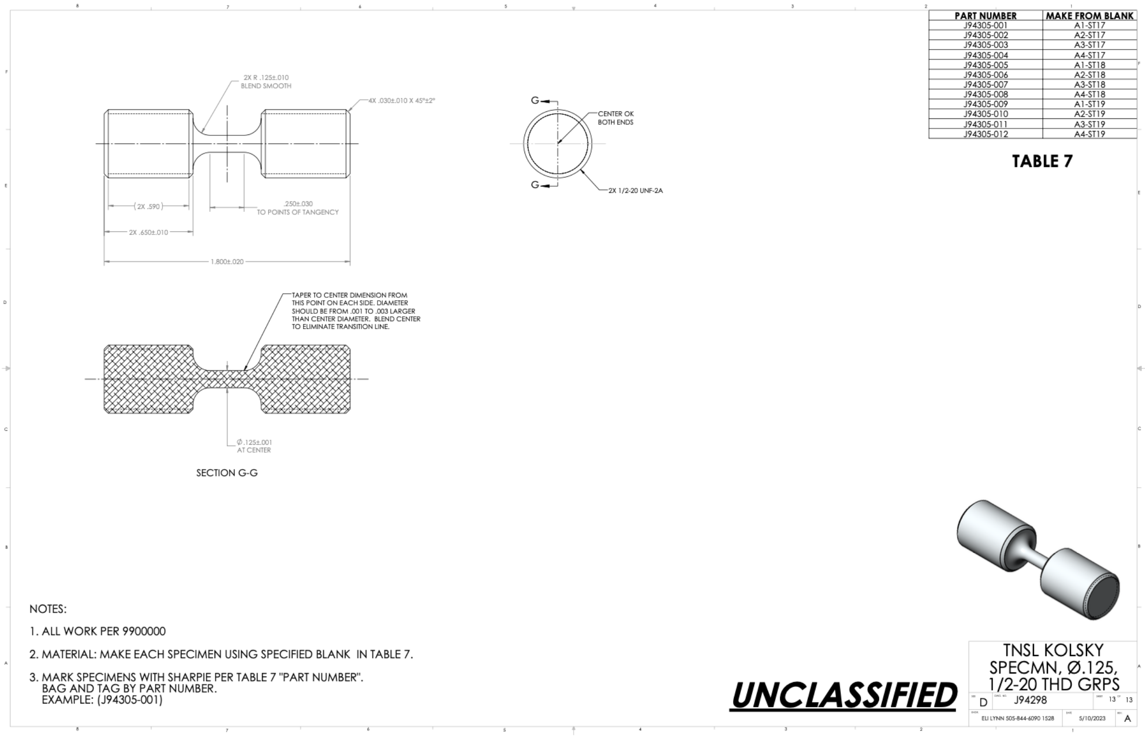

PART NUMBER	MAKE FROM BLANK
J94305-001	A1-ST17
J94305-002	A2-ST17
J94305-003	A3-ST17
J94305-004	A4-ST17
J94305-005	A1-ST18
J94305-006	A2-ST18
J94305-007	A3-ST18
J94305-008	A4-ST18
J94305-009	A1-ST19
J94305-010	A2-ST19
J94305-011	A3-ST19
J94305-012	A4-ST19

TABLE 7

NOTES:

1. ALL WORK PER 9900000
2. MATERIAL: MAKE EACH SPECIMEN USING SPECIFIED BLANK IN TABLE 7.
3. MARK SPECIMENS WITH SHARPIE PER TABLE 7 "PART NUMBER".
   BAG AND TAG BY PART NUMBER.
   EXAMPLE: (J94305-001)

C: Calibrated Material Input Deck

```
#{psi2pa = 6894.76}
# {ft2inch = 12}
# {inch2m = 0.0254}
# {lbf2n = 4.442}


# NOTE: coordinate system is different for hat and notch/tension


#begin rectangular coordinate system rcs
# origin = 0. 0. 0.
# z point = 0. 0. 1.
# xz point = 1. 0. 1.
#end rectangular coordinate system rcs


begin property specification for material Al7075_PLH
        density = {2.5e-4*lbf2n/(inch2m^4)}
```

```
begin parameters for model hill_plasticity
    youngs modulus = {10.4e6 * psi2pa}
    poissons ratio = 0.33
 coordinate system = rcs
 r11 = 1.
 r22 = 1.
 r33 = 1.
 r12 = 1.
 r23 = 0.83
 r31 = 0.83
    yield stress = {73969.*psi2pa}
    hardening model = flow_stress_parameter
    isotropic hardening model = power_law_parameter
 hardening constant = {57289.*psi2pa}
 hardening exponent = 0.33

    yield stress function       = f_ys
    hardening constant function = f_hard
    hardening exponent function = f_exp

    rate multiplier = johnson_cook
    rate constant   = 0.002
    reference rate  = {0.125e-3/0.750}

    thermal softening model = adiabatic
    specific heat          = 900
    beta_tq                = 0.8

    failure model = modular_failure
    critical failure parameter = 0.5
```

```
           #critical failure parameter function = f_fail_crit
        temperature fail multiplier = user_defined
        temperature fail multiplier function = f_fail_crit

        rate fail multiplier = johnson_cook
        johnson cook d4 = -0.015

           pressure multiplier = wilkins
                 wilkins alpha    = 7.85
             wilkins pressure = 4.0e9
           lode angle multiplier = wilkins
             wilkins beta  = 1.25

          end parameters for model hill_plasticity
        end property specification for material Al7075_PLH

#begin function f_fail_crit
#        type is piecewise linear
#      abscissa = temperature
#        begin values
#        20.0    {0.5/0.5}
#        50.0    {1.15/0.5}
#        100.0   {4.1/0.5}
#        end values
#end function f_fail_crit

begin function f_fail_crit
        type is piecewise linear
     abscissa = temperature
        begin values
```

```
        20.0    {1.0}
        50.0    {1./1.08}
        100.0   {1./3.5}
        end values
end function f_fail_crit

begin function f_ys
        type is piecewise linear
        begin values
        20    1.0
        50    {404./510.}
        100   {253./510.}
        end values
end function f_ys

begin function f_hard
        type is piecewise linear
        begin values
        20    1.0
        50    {426./395.}
        100   {476./395.}
        end values
end function f_hard

begin function f_exp
        type is piecewise linear
        begin values
        20    1.0
        50    {0.196/0.33}
        100   {0.131/0.33}
```

```
        end values
end function f_exp
```